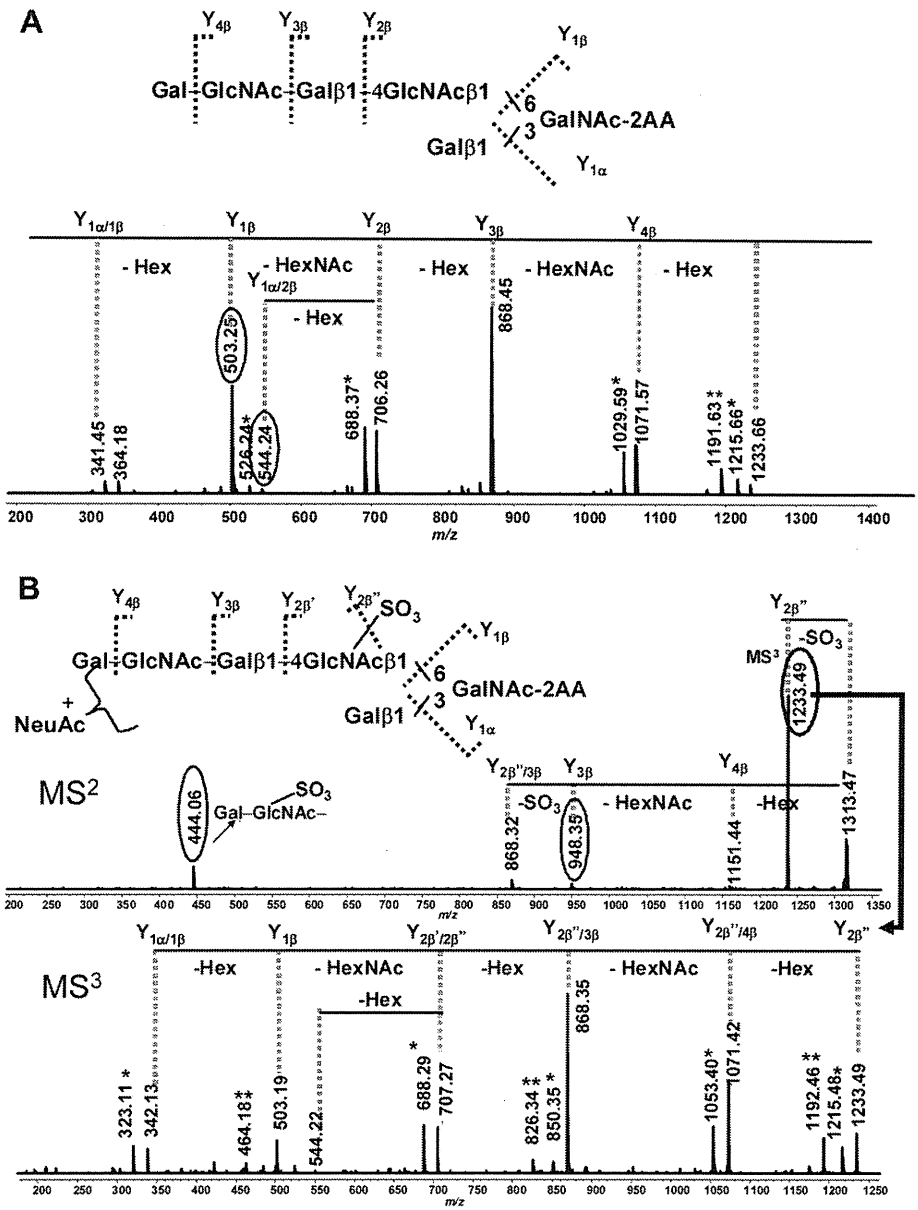

Fig.4. MS/MS analysis of mucin-type glycans derived from HCT116 cells. (A) Polylactosaminyl mucin-type glycan observed at *m/z* 1233. (B) Sulfated mucin-type glycan observed at *m/z* 1604.

could easily discriminate these cells. K562 cells contained ΔdiCS-4S as the major component. In contrast, ΔdiHS-0S was the major component in U937 cells. U937 cells also contained ΔdiCS-4S, but the relative abundance of this unsaturated disaccharide was low. Jurkat cells expressed extremely large amount of Tn antigen. GAGs in Jurkat cells showed profiles similar to those observed in U937 cells. HL-60 cells expressed core 2 mucin-type glycans abundantly. In addition, polylactosaminyl and fucosylated mucin-type glycans were also observed in HL-60 cells. A feature of HL-60 cells is that the cells express elongated mucin-type glycans in comparison with other leukemia cells. ΔdiCS-0S was the major component in HL-60 cells. This means that low-sulfated GAGs were abundant in HL-60 cells.

Fig. 8 shows the results on the characterization of six epithelial cancer cell lines. Mucin-type glycan profiles in epithelial cancer cell lines except PANC1 cells are generally more complex than those of leukemia cancer cells. This means that characterization of mucin-type glycans on epithelial cancer cells will be a powerful tool for correlating with their biological characteristics such as tumorigenesis ability. Sialyl-T and disialyl-T antigens were commonly observed in all cancer cells, although their relative abundances were diverse among cells. However, all cancer cells scarcely expressed core 3 and core 4 structures. These data are well correlated with the reports on down-regulation of these glycans in various tumor tissues [21,22]. Profiles of GAGs also gave interesting results. Relative abundances of HA in epithelial cancer cells were commonly higher than those in leukemia cells. In addition, relative abundances of ΔdiHS-0S also showed higher values than those observed for leukemia cells. These data indicate that sulfation level of HS is significantly low in cancer cell lines. Recently, some research groups reported that HS sulfatases (SULF) are overexpressed in subsets of multiple tumors [41–43]. SULF2 overexpressed in tumor tissues was associated with tumor prognosis [42,44]. These reports indicate that sulfation level of HS is decreased in certain cancer cell lines. Our results are well correlated with these observations. PANC1 cells (poorly differentiated pancreatic cancer cells) expressed sialyl-T and disialyl-T as the major mucin-type glycans. The elongated mucin-type glycans were not

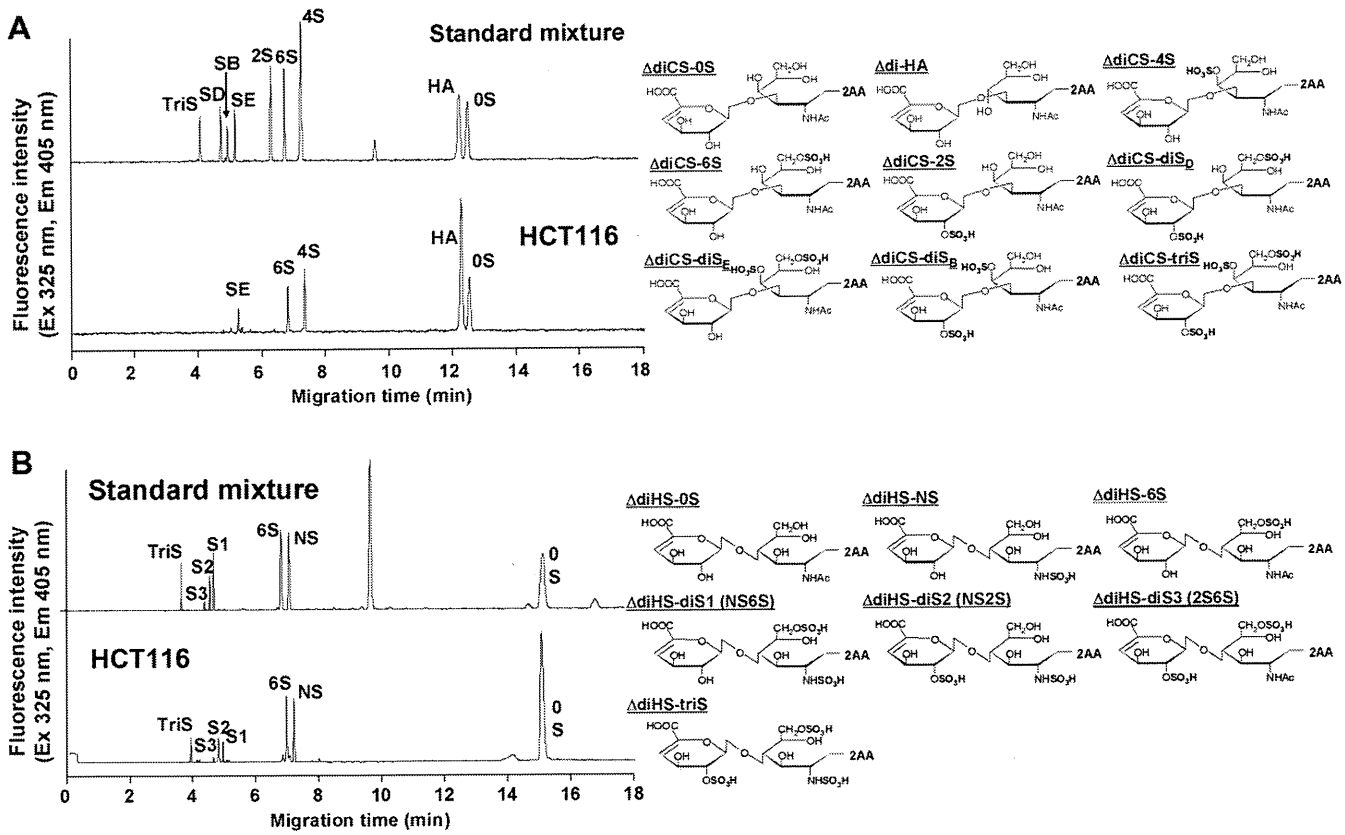

Fig.5. Analysis of unsaturated disaccharides from GAG fractions. 2AA-labeled unsaturated disaccharides of HA and CS (A) and of HS (B) in HCT116 cells were analyzed by CE. Analytical conditions: capillary, fused silica (40 cm × 50 μm i.d); running buffer, 100 mM Tris–phosphate (pH 3.0); applied voltage, 25 kV; injection, pressure method (1.0 psi for 10 s); temperature, 25 °C; detection, He-Cd laser-induced fluorescent detection (excitation 325 nm, emission 405 nm). Abbreviations of unsaturated disaccharide: (A) Unsaturated chondroitin and hyaluronic acid disaccharide: 0S, ΔdiCS-0S (12.8 min); HA, ΔdiHA (12.3 min); 4S, ΔdiCS-4S (7.4 min); 6S, ΔdiCS-6S (6.8 min); 2S, ΔdiCS-2S (6.5 min); SD, ΔdiCS-diS$_D$ (4.8 min); SE, ΔdiCS-diS$_E$ (5.2 min); SB, ΔdiCS-diS$_B$ (5.0 min); TriS, ΔdiCS-triS (4.1 min). (B) Unsaturated heparan sulfate disaccharide: 0S, ΔdiHS-0S (15.3 min); NS, ΔdiHS-NS (7.2 min); 6S, ΔdiHS-6S (6.8 min); S1, ΔdiHS-diS1 (5.0 min); S2, ΔdiHS-diS2 (4.9 min); S3, ΔdiHS-diS3 (4.8 min); TriS, ΔdiHS-TriS (4.0 min).

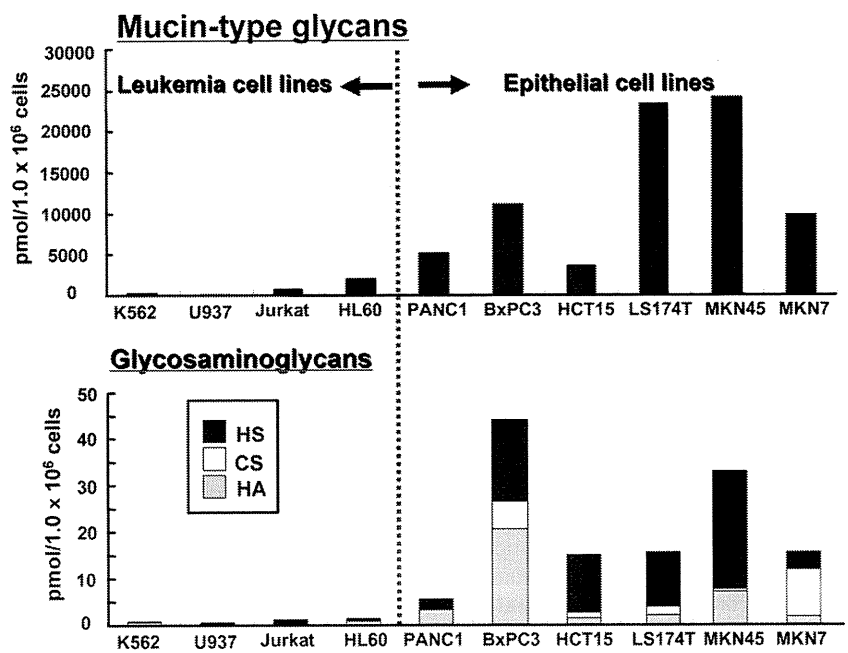

Fig.6. Comparison of the amounts of mucin-type glycans and GAGs expressed on cancer cells. The amounts of the expressed mucin-type glycans and GAGs were calculated from the peak areas observed by NP-HPLC and CE, respectively.

observed in PANC1 cells. Because PANC1 cells lack core 2 β-1,6-*N*-acetylglucosaminyltransferase, which is required for elongation of the mucin-type glycans [45], these observations suggest that tumor-associated epitopes on mucin core proteins expressed on

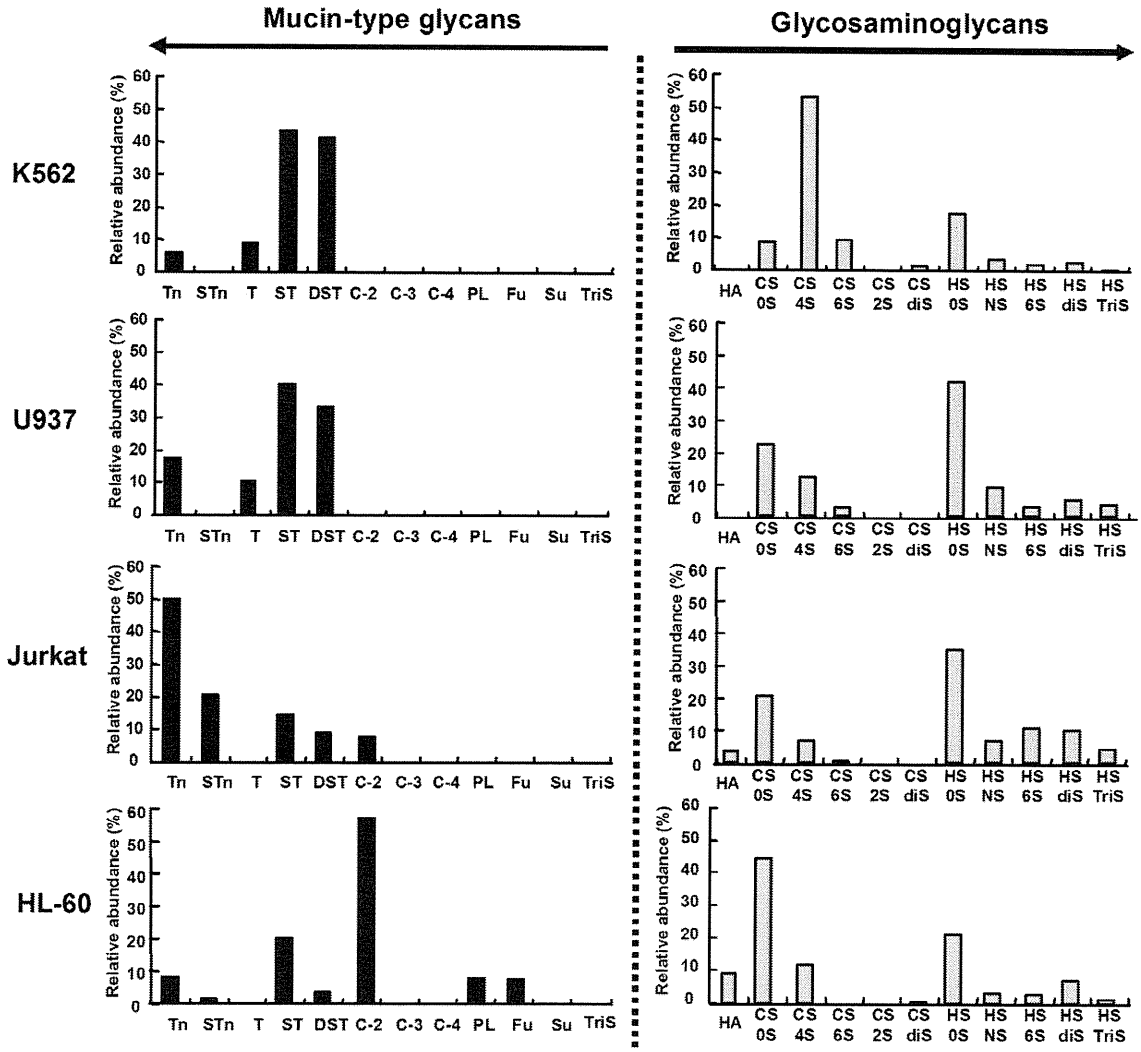

Fig.7. Characterization of four leukemia cell lines. The contents of mucin-type glycans and GAGs are displayed as black bars and gray bars, respectively. Relative abundances of mucin-type glycans and unsaturated disaccharides were calculated from the peak areas observed by NP–HPLC and CE, respectively. Abbreviations: Tn, Tn antigen; STn, sialyl-Tn antigen; T, T antigen; ST, sialyl-T antigen; DST, disialyl-T antigen; C-2, core 2 structure; C-3, core 3 structure; C-4, core 4 structure; PL, polylactosamine-type structure; Fu, fucosylated structure; Su, sulfated structure; TriS, trisialylated structure; HA, Δdi-HA; CS-0S, ΔdiCS-0S; CS-4S, ΔdiCS-4S; CS-6S, ΔdiCS-6S; CS-2S, ΔdiCS-2S; CS-diS, disulfated unsaturated disaccharides of CS; HS-0S, ΔdiHS-0S; HS-NS, ΔdiHS-NS; HS-6S, ΔdiHS-6S; HS-diS, disulfated unsaturated disaccharides of HS; HS-TriS, trisulfated unsaturated disaccharides of HS.

PANC1 cells are exposed to the external environment. Mucin-type glycans of BxPC3 cells were obviously different from those of PANC1 cells. Core 2 structure was the major glycan in BxPC3 cells, and its modified structures (i.e., polylactosaminyl structure and fucosylated glycans) were also observed in BxPC3 cells. Mare and Trinchera reported that BxPC3 cells expressed polylactosamine-type glycans [46]. The profiles of GAGs of PANC1 cells are quite interesting, and only HA and low-sulfated HS (HS0S) were observed. HA and HS were also the major GAGs in BxPC3 cells (moderately differentiated pancreatic cancer cell lines), and profiles similar to those of PANC1 cells were reported. The expression level of HA was increased in pancreatic cancer cells [35], and its increase was a risk factor for tumor proliferation and metastasis [36,47]. In addition, BxPC3 cells obviously expressed CS, which was not observed in PANC1 cells. Sulfated mucin-type glycans were characteristically observed in colon cancer cell lines, HCT15 and LS174T. HCT15 cells expressed core 2 and polylactosamine-type glycans as the major mucin-type glycans. In addition, sialyl-T and disialyl-T were abundant in HCT15 cells. Most of the abundant mucin-type glycans in LS174T cells were fucosylated. LS174T cells also expressed large amounts of Tn antigen and polylactosamine-type glycans. This is a specific feature of LS174T cells in which both truncated and extended glycans were present. Both HCT15 and LS174T cells contained low-sulfated HS (HS0S) as the major GAGs. In contrast, the level of HS sulfation in HCT15 cells was a little bit higher than that observed in LS174T cells. However, relative abundance of ΔdiCS-6S in LS174T cells was higher than that in HCT15 cells. We previously reported that the profiles of mucin-type glycans were dramatically changed with differentiation stages of gastric cancer cell lines [38]. Poorly differentiated gastric cancer cells (MKN45 cells) expressed large amounts of extended polylactosamine-type glycans with molecular masses greater than 6000 [38]. In addition, trisialylated mucin-type glycans were characteristically observed in MKN45 cells. In contrast, polylactosamine-type glycans were not observed in well-differentiated gastric cancer cells (MKN7 cells). In MKN7 cells, glycans of core 2 structure were observed abundantly. This means that elongation of core 2 structure to polylactosamine-type glycan is suppressed in MKN7 cells, although further studies on the related synthetic enzymes are required. Profiles of GAGs in these two gastric cancer cells were quite different. HA and low-sulfated HS (HS0S) were abundant, but CSs were scarcely observed in MKN45 cells. In contrast, CSs were the major GAGs in MKN7 cells. Relative abundance of ΔdiCS-4S was especially distinct in MKN7 cells.

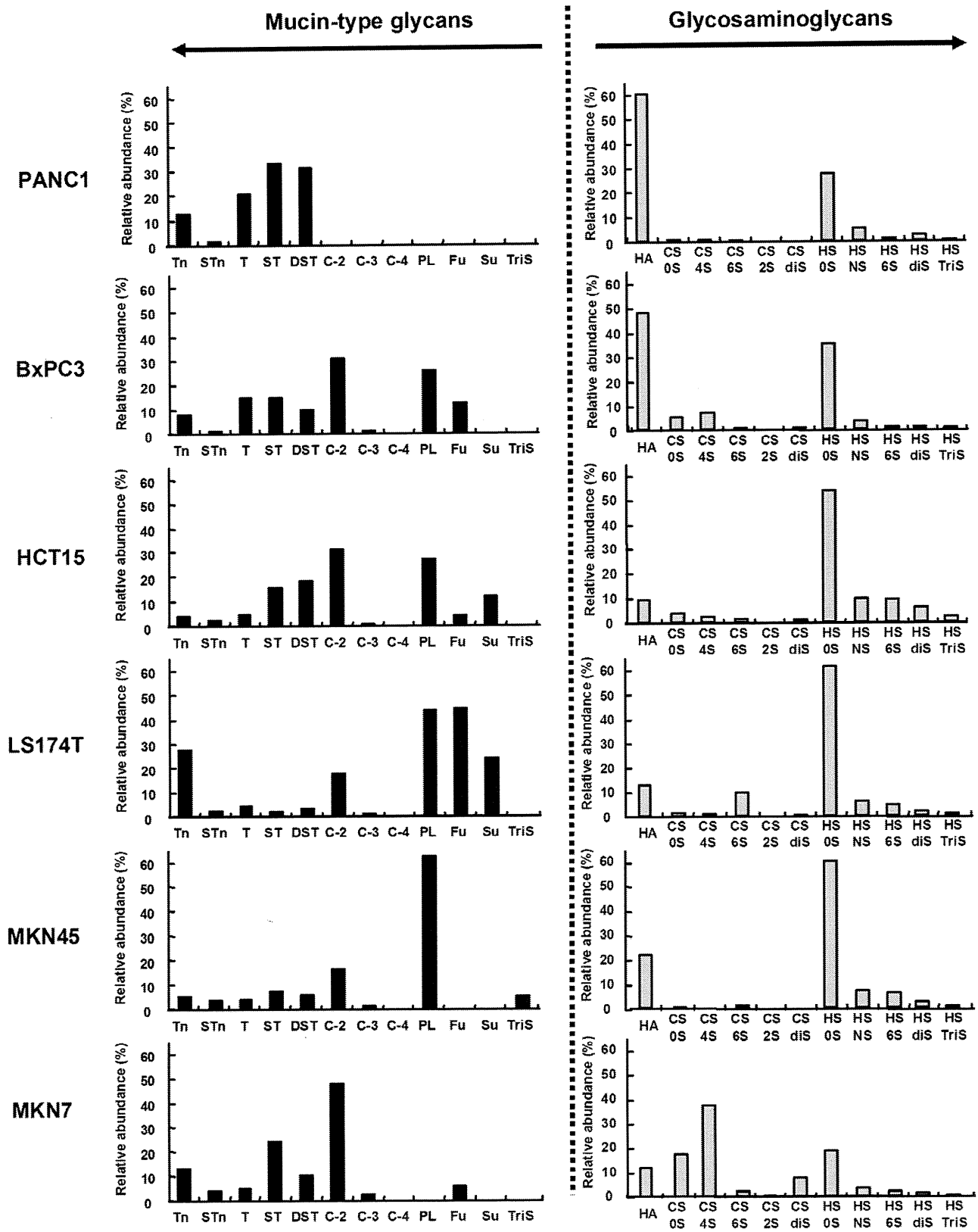

Fig.8. Characterization of six epithelial cancer cell lines. The contents of mucin-type glycans and GAGs are displayed as black bars and gray bars, respectively. Calculation of relative abundances and abbreviations are the same as in Fig. 7.

Although further studies are required, these results may indicate that GAGs play an important role in differentiation of gastric cancer cells.

As described above, it was revealed that our methods are useful to characterize the various cancer cell lines. In the future, we will apply these methods to compare *O*-glycan profiles between cancer

cells and normal cells and to reveal the tumor-specific alterations of *O*-glycan profiles.

Conclusion

We have developed an automatic system for releasing *O*-glycans from glycoproteins and applied the methods to the analysis of the released mucin-type glycans. In the current study, we developed methods for one-pot analysis of mucin-type glycans and GAGs. Serotonin affinity chromatography for group separation of mucin-type glycans based on the number of sialic acid residues [38] is also useful for collection of GAGs. As shown in Fig. 1, GAGs were strongly retained on the serotonin-immobilized column, and group separation of GAGs and mucin-type glycans was easily achieved. After collection of these glycans, mucin-type glycans were conveniently analyzed by MALDI–TOF MS and HPLC, and GAGs could be analyzed by CE as a mixture of unsaturated disaccharides after digestion with specific eliminases.

Two leukemia cancer cell lines (U937 and K562) showed similar profiles of mucin-type glycans and could not be discriminated only by comparing mucin-type glycans. However, GAG profiles showed obviously distinct characteristics (Fig. 7). In contrast, pancreatic cancer cell lines (PANC1 and BxPC3) showed similar GAG profiles but quite different mucin-type glycan profiles (Fig. 8). We also revealed that the profiles of GAGs as well as mucin-type glycans were dramatically altered at different differentiation stages of cancer cells, as determined by the analysis of MKN45 and MKN7 cells.

Based on these results, the current techniques will be useful to discover the novel biomarkers for diseases. However, the relationship between biological characteristics and *O*-glycan profiles observed in cancer cells might not be the same with that observed in actual physiological conditions. Therefore, to discover the practical glycan biomarkers for diagnosis of tumors, our method needs to be applied to the clinical samples such as serum or tissue samples. We are now applying the current methods to various kinds of biological samples. Furthermore, we are also developing methods for identification of proteins carrying specific glycans. These results will be shown in future publications.

Appendix A. Supplementary data

Supplementary data associated with this article can be found, in the online version, at doi:10.1016/j.ab.2011.12.017.

References

[1] S. Kamoda, M. Nakano, R. Ishikawa, S. Suzuki, K. Kakehi, Rapid and sensitive screening of *N*-glycans as 9-fluorenylmethyl derivatives by high-performance liquid chromatography: a method which can recover free oligosaccharides after analysis, J. Proteome Res. 4 (2005) 146–152.

[2] R. Naka, S. Kamoda, A. Ishizuka, M. Kinoshita, K. Kakehi, Analysis of total *N*-glycans in cell membrane fractions of cancer cells using a combination of serotonin affinity chromatography and normal phase chromatography, J. Proteome Res. 5 (2006) 88–97.

[3] S. Kamoda, R. Ishikawa, K. Kakehi, Capillary electrophoresis with laser-induced fluorescence detection for detailed studies on N-linked oligosaccharide profile of therapeutic recombinant monoclonal antibodies, J. Chromatogr. A 1133 (2006) 332–339.

[4] K. Kakehi, A. Susami, A. Taga, S. Suzuki, S. Honda, High-performance capillary electrophoresis of O-glycosidically linked sialic acid-containing oligosaccharides in glycoproteins as their alditol derivatives with low-wavelength UV monitoring, J. Chromatogr. A 680 (1994) 209–215.

[5] B.L. Schulz, N.H. Packer, N.G. Karlsson, Small-scale analysis of O-linked oligosaccharides from glycoproteins and mucins separated by gel electrophoresis, Anal. Chem. 74 (2002) 6088–6097.

[6] M. Backstrom, K.A. Thomsson, H. Karlsson, G.C. Hansson, Sensitive liquid chromatography–electrospray mass spectrometry allows for the analysis of the O-glycosylation of immunoprecipitated proteins from cells or tissues: application to MUC1 glycosylation in cancer, J. Proteome Res. 8 (2009) 538–545.

[7] L. Royle, T.S. Mattu, E. Hart, J.I. Langridge, A.H. Merry, N. Murphy, D.J. Harvey, R.A. Dwek, P.M. Rudd, An analytical and structural database provides a strategy for sequencing *O*-glycans from microgram quantities of glycoproteins, Anal. Biochem. 304 (2002) 70–90.

[8] Y. Huang, Y. Mechref, M.V. Novotny, Microscale nonreductive release of O-linked glycans for subsequent analysis through MALDI mass spectrometry and capillary electrophoresis, Anal. Chem. 73 (2001) 6063–6069.

[9] K. Yamada, S. Hyodo, Y.K. Matsuno, M. Kinoshita, S.Z. Maruyama, Y.S. Osaka, E. Casal, Y.C. Lee, K. Kakehi, Rapid and sensitive analysis of mucin-type glycans using an in-line flow glycan-releasing apparatus, Anal. Biochem. 371 (2007) 52–61.

[10] K. Yamada, K. Kakehi, Recent advances in the analysis of carbohydrates for biomedical use, J. Pharm. Biomed. Anal. 55 (2011) 702–727.

[11] K. Yamada, S. Hyodo, M. Kinoshita, T. Hayakawa, K. Kakehi, Hyphenated technique for releasing and MALDI MS analysis of *O*-glycans in mucin-type glycoprotein samples, Anal. Chem. 82 (2010) 7436–7443.

[12] Y.K. Matsuno, K. Yamada, A. Tanabe, M. Kinoshita, S.Z. Maruyama, Y.S. Osaka, T. Masuko, K. Kakehi, Development of an apparatus for rapid release of oligosaccharides at the glycosaminoglycan–protein linkage region in chondroitin sulfate-type proteoglycans, Anal. Biochem. 362 (2007) 245–257.

[13] R.S. Aquino, E.S. Lee, P.W. Park, Diverse functions of glycosaminoglycans in infectious diseases, Prog. Mol. Biol. Transl. Sci. 93 (2010) 373–394.

[14] S. Mizuguchi, T. Uyama, H. Kitagawa, K.H. Nomura, K. Dejima, K. Gengyo-Ando, S. Mitani, K. Sugahara, K. Nomura, Chondroitin proteoglycans are involved in cell division of *Caenorhabditis elegans*, Nature 423 (2003) 443–448.

[15] A. Guzman-Aranguez, P. Argueso, Structure and biological roles of mucin-type *O*-glycans at the ocular surface, Ocul. Surf. 8 (2010) 8–17.

[16] N.L. Perillo, K.E. Pace, J.J. Seilhamer, L.G. Baum, Apoptosis of T cells mediated by galectin-1, Nature 378 (1995) 736–739.

[17] S.J. Storr, L. Royle, C.J. Chapman, U.M. Hamid, J.F. Robertson, A. Murray, R.A. Dwek, P.M. Rudd, The O-linked glycosylation of secretory/shed MUC1 from an advanced breast cancer patient's serum, Glycobiology 18 (2008) 456–462.

[18] P.H. Jensen, D. Kolarich, N.H. Packer, Mucin-type O-glycosylation – putting the pieces together, FEBS J. 277 (2010) 81–94.

[19] Y. Mechref, M.V. Novotny, Structural investigations of glycoconjugates at high sensitivity, Chem. Rev. 102 (2002) 321–369.

[20] H.J. An, S.R. Kronewitter, M.L. de Leoz, C.B. Lebrilla, Glycomics and disease markers, Curr. Opin. Chem. Biol. 13 (2009) 601–607.

[21] S.H. Lee, M. Fukuda, Core 3 glycan as tumor suppressor, Methods Enzymol. 479 (2010) 143–154.

[22] T. Iwai, T. Kudo, R. Kawamoto, T. Kubota, A. Togayachi, T. Hiruma, T. Okada, T. Kawamoto, K. Morozumi, H. Narimatsu, Core 3 synthase is down-regulated in colon carcinoma and profoundly suppresses the metastatic potential of carcinoma cells, Proc. Natl Acad. Sci. USA 102 (2005) 4572–4577.

[23] I. Brockhausen, Pathways of *O*-glycan biosynthesis in cancer cells, Biochim. Biophys. Acta 1473 (1999) 67–95.

[24] I. Brockhausen, Sulphotransferases acting on mucin-type oligosaccharides, Biochem. Soc. Trans. 31 (2003) 318–325.

[25] I. Brockhausen, Glycodynamics of mucin biosynthesis in gastrointestinal tumor cells, Adv. Exp. Med. Biol. 535 (2003) 163–188.

[26] G.F. Springer, T and Tn, general carcinoma autoantigens, Science 224 (1984) 1198–1206.

[27] S. Nakamori, M. Kameyama, S. Imaoka, H. Furukawa, O. Ishikawa, Y. Sasaki, T. Kabuto, T. Iwanaga, Y. Matsushita, T. Irimura, Increased expression of sialyl Lewis^x antigen correlates with poor survival in patients with colorectal carcinoma: clinicopathological and immunohistochemical study, Cancer Res. 53 (1993) 3632–3637.

[28] C. Hanski, E. Klussmann, J. Wang, C. Bohm, D. Ogorek, M.L. Hanski, S. Kruger-Krasagakes, J. Eberle, A. Schmitt-Graff, E.O. Riecken, Fucosyltransferase III and sialyl-Le^x expression correlate in cultured colon carcinoma cells but not in colon carcinoma tissue, Glycoconj. J. 13 (1996) 727–733.

[29] N. Kojima, K. Handa, W. Newman, S. Hakomori, Inhibition of selectin-dependent tumor cell adhesion to endothelial cells and platelets by blocking O-glycosylation of these cells, Biochem. Biophys. Res. Commun. 182 (1992) 1288–1295.

[30] Y.H. Teng, P.H. Tan, S.J. Chia, N.A. Zam, W.K. Lau, C.W. Cheng, B.H. Bay, G.W. Yip, Increased expression of non-sulfated chondroitin correlates with adverse clinicopathological parameters in prostate cancer, Mod. Pathol. 21 (2008) 893–901.

[31] H. Nakanishi, K. Oguri, K. Yoshida, N. Itano, K. Takenaga, T. Kazama, A. Yoshida, M. Okayama, Structural differences between heparan sulphates of proteoglycan involved in the formation of basement membranes in vivo by Lewis-lung-carcinoma-derived cloned cells with different metastatic potentials, Biochem. J. 288 (1992) 215–224.

[32] K. Raman, B. Kuberan, Chemical tumor biology of heparan sulfate proteoglycans, Curr. Chem. Biol. 4 (2010) 20–31.

[33] R.D. Sanderson, Y. Yang, T. Kelly, V. MacLeod, Y. Dai, A. Theus, Enzymatic remodeling of heparan sulfate proteoglycans within the tumor microenvironment: Growth regulation and the prospect of new cancer therapies, J. Cell. Biochem. 96 (2005) 897–905.

[34] R. Sasisekharan, S. Ernst, G. Venkataraman, On the regulation of fibroblast growth factor activity by heparin-like glycosaminoglycans, Angiogenesis 1 (1997) 45–54.

[35] A.D. Theocharis, M.E. Tsara, N. Papageorgacopoulou, D.D. Karavias, D.A. Theocharis, Pancreatic carcinoma is characterized by elevated content of

hyaluronan and chondroitin sulfate with altered disaccharide composition, Biochim. Biophys. Acta 1502 (2000) 201–206.
[36] H. Morohashi, A. Kon, M. Nakai, M. Yamaguchi, I. Kakizaki, S. Yoshihara, M. Sasaki, K. Takagaki, Study of hyaluronan synthase inhibitor, 4-methylumbelliferone derivatives, on human pancreatic cancer cell (KP1-NL), Biochem. Biophys. Res. Commun. 345 (2006) 1454–1459.
[37] F.J. Vizoso, J.M. del Casar, M.D. Corte, I. Garcia, M.G. Corte, A. Alvarez, J.L. Garcia-Muniz, Significance of cytosolic hyaluronan levels in gastric cancer, Eur. J. Surg. Oncol. 30 (2004) 318–324.
[38] K. Yamada, M. Kinoshita, T. Hayakawa, S. Nakaya, K. Kakehi, Comparative studies on the structural features of *O*-glycans between leukemia and epithelial cell lines, J. Proteome Res. 8 (2009) 521–537.
[39] A. Ishizuka, Y. Hashimto, R. Naka, M. Kinoshita, K. Kakehi, J. Seino, Y. Funakoshi, T. Suzuki, A. Kameyama, H. Narimatsu, Accumulation of free complex-type *N*-glycans in MKN7 and MKN45 stomach cancer cells, Biochem. J. 413 (2008) 227–237.
[40] A. Seko, K. Nagata, S. Yonezawa, K. Yamashita, Ectopic expression of a GlcNAc 6-*O*-sulfotransferase, GlcNAc6ST-2, in colonic mucinous adenocarcinoma, Glycobiology 12 (2002) 379–388.
[41] N.P. Castro, C.A. Osorio, C. Torres, E.P. Bastos, M. Mourao-Neto, F.A. Soares, H.P. Brentani, D.M. Carraro, Evidence that molecular changes in cells occur before morphological alterations during the progression of breast ductal carcinoma, Breast Cancer Res. 10 (2008) R87.
[42] J.P. Lai, D.S. Sandhu, C. Yu, T. Han, C.D. Moser, K.K. Jackson, R.B. Guerrero, I. Aderca, H. Isomoto, M.M. Garrity-Park, H. Zou, A.M. Shire, D.M. Nagorney, S.O. Sanderson, A.A. Adjei, J.S. Lee, S.S. Thorgeirsson, L.R. Roberts, Sulfatase 2 up-regulates glypican 3, promotes fibroblast growth factor signaling, and decreases survival in hepatocellular carcinoma, Hepatology 47 (2008) 1211–1222.
[43] Y. Kudo, I. Ogawa, S. Kitajima, M. Kitagawa, H. Kawai, P.M. Gaffney, M. Miyauchi, T. Takata, Periostin promotes invasion and anchorage-independent growth in the metastatic process of head and neck cancer, Cancer Res. 66 (2006) 6928–6935.
[44] H. Lemjabbar-Alaoui, A. van Zante, M.S. Singer, Q. Xue, Y.Q. Wang, D. Tsay, B. He, D.M. Jablons, S.D. Rosen, Sulf-2, a heparan sulfate endosulfatase, promotes human lung carcinogenesis, Oncogene 29 (2010) 635–646.
[45] P.V. Beum, J. Singh, M. Burdick, M.A. Hollingsworth, P.W. Cheng, Expression of core 2β-1,6-*N*-acetylglucosaminyltransferase in a human pancreatic cancer cell line results in altered expression of MUC1 tumor-associated epitopes, J. Biol. Chem. 274 (1999) 24641–24648.
[46] L. Mare, M. Trinchera, Suppression of β-1,3-galactosyltransferase β-3Gal-T5 in cancer cells reduces sialyl-Lewis^a and enhances poly-*N*-acetyllactosamines and sialyl-Lewis^x on *O*-glycans, Eur. J. Biochem. 271 (2004) 186–194.
[47] C. Pellizzaro, A. Speranza, S. Zorzet, I. Crucil, G. Sava, I. Scarlata, S. Cantoni, M. Fedeli, D. Coradini, Inhibition of human pancreatic cell line MIA PaCa2 proliferation by HA-But, a hyaluronic butyric ester: a preliminary report, Pancreas 36 (2008) e15–e23.

Biomaterials 34 (2013) 1781–1789

Contents lists available at SciVerse ScienceDirect

Biomaterials

journal homepage: www.elsevier.com/locate/biomaterials

3D spheroid culture of hESC/hiPSC-derived hepatocyte-like cells for drug toxicity testing

Kazuo Takayama [a,b], Kenji Kawabata [b,c], Yasuhito Nagamoto [a,b], Keisuke Kishimoto [a,b], Katsuhisa Tashiro [b], Fuminori Sakurai [a], Masashi Tachibana [a], Katsuhiro Kanda [d], Takao Hayakawa [e], Miho Kusuda Furue [f,g], Hiroyuki Mizuguchi [a,b,h,*]

[a] Laboratory of Biochemistry and Molecular Biology, Graduate School of Pharmaceutical Sciences, Osaka University, Osaka 565-0871, Japan
[b] Laboratory of Stem Cell Regulation, National Institute of Biomedical Innovation, Osaka 567-0085, Japan
[c] Laboratory of Biomedical Innovation, Graduate School of Pharmaceutical Sciences, Osaka University, Osaka 565-0871, Japan
[d] Pharma Business Project, Corporate Projects Center, Corporate Strategy Division, Hitachi High-Technologies Corporation, Ibaraki 312-8504, Japan
[e] Pharmaceutical Research and Technology Institute, Kinki University, Osaka 577-8502, Japan
[f] Laboratory of Embryonic Stem Cell Cultures, Department of Disease Bioresources Research, National Institute of Biomedical Innovation, Osaka 567-0085, Japan
[g] Department of Embryonic Stem Cell Research, Field of Stem Cell Reseach, Institute for Frontier Medical Sciences, Kyoto University, Kyoto 606-8507, Japan
[h] The Center for Advanced Medical Engineering and Informatics, Osaka University, Osaka 565-0871, Japan

ARTICLE INFO

Article history:
Received 11 September 2012
Accepted 20 November 2012
Available online 8 December 2012

Keywords:
Hepatocyte-like cell
Human ES cell
Human iPS cell
Nanopillar plate
Drug screening

ABSTRACT

Although it is expected that hepatocyte-like cells differentiated from human embryonic stem (ES) cells or induced pluripotent stem (iPS) cells will be utilized in drug toxicity testing, the actual applicability of hepatocyte-like cells in this context has not been well examined so far. To generate mature hepatocyte-like cells that would be applicable for drug toxicity testing, we established a hepatocyte differentiation method that employs not only stage-specific transient overexpression of hepatocyte-related transcription factors but also a three-dimensional spheroid culture system using a Nanopillar Plate. We succeeded in establishing protocol that could generate more matured hepatocyte-like cells than our previous protocol. In addition, our hepatocyte-like cells could sensitively predict drug-induced hepatotoxicity, including reactive metabolite-mediated toxicity. In conclusion, our hepatocyte-like cells differentiated from human ES cells or iPS cells have potential to be applied in drug toxicity testing.

1. Introduction

Hepatocyte-like cells that are generated from human embryonic stem cells (hESCs) [1] or human induced pluripotent stem cells (hiPSCs) [2] are expected to be used in drug screening instead of primary (or cryopreserved) human hepatocytes (PHs). We recently demonstrated that stage-specific transient transduction of transcription factors, in addition to treatment with optimal growth factors and cytokines, is useful for promoting hepatic differentiation [3–6]. The hepatocyte-like cells, which have many hepatocyte characteristics (the abilities to uptake low-density lipoprotein and Indocyanine green, store glycogen, and synthesize urea) and drug metabolism capacity, were generated from hESCs/hiPSCs by combinational transduction of FOXA2 and HNF1α [6]. However, further maturation of the hepatocyte-like cells is required because their hepatic characteristics, such as drug metabolism capacity, are lower than those of PHs [6].

To promote further maturation of the hepatocyte-like cells, we subjected them to three-dimensional (3D) spheroid cultures. It is known that various 3D culture conditions (such as Algimatrix scaffolds [7], cell sheet technology [8], galactose-carrying substrata [9], and basement membrane substratum [10]) are useful for the maturation of the hepatocyte-like cells. Nanopillar Plate technology [11] used in the present study makes it easy to control the configuration of the spheroids. The Nanopillar Plate has an arrayed μm-scale hole structure at the bottom of each well, and nanopillars were aligned further at the bottom of the respective holes. The seeded cells evenly drop into the holes, then migrate and aggregate on top surface of the nanopillars, thus likely to form the uniform spheroids in each hole. Not only 3D spheroid cultures [12] but also Matrigel overlay cultures [13] are useful for maintaining the hepatocyte characteristics of PHs. Therefore, we employed both 3D

* Corresponding author. Laboratory of Biochemistry and Molecular Biology, Graduate School of Pharmaceutical Sciences, Osaka University, 1-6 Yamadaoka, Suita, Osaka 565-0871, Japan. Tel.: +81 6 6879 8185; fax: +81 6 6879 8186.
E-mail address: mizuguch@phs.osaka-u.ac.jp (H. Mizuguchi).

0142-9612/$ – see front matter © 2012 Elsevier Ltd. All rights reserved.
http://dx.doi.org/10.1016/j.biomaterials.2012.11.029

spheroid culture and Matrigel overlay culture systems to promote hepatocyte maturation of the hepatocyte-like cells.

The hepatocyte-like cells generated from hESCs/hiPSCs are expected to be used in drug development. To the best of our knowledge, however, few studies have tried to predict widespread drug-induced cytotoxicity *in vitro* using the hepatocyte-like cells. To precisely determine the applicability of the hepatocyte-like cells to drug screening, it is necessary to investigate the responses of these hepatocyte-like cells to many kinds of hepatotoxic drugs.

In this study, 3D spheroid and Matrigel overlay cultures of the hepatocyte-like cells were performed to promote hepatocyte maturation. The gene expression analysis of cytochrome P450 (CYP) enzymes, conjugating enzymes, hepatic transporters, and hepatic nuclear receptors in the 3D spheroid-cultured hESC- or hiPSC-derived hepatocyte-like cells (3D ES-hepa or 3D iPS-hepa), were analyzed. In addition, CYP induction potency and drug metabolism capacity were estimated in the 3D ES/iPS-hepa. To determine the suitability of these cells for drug screening, we examined whether the drug-induced cytotoxicity is induced by treatment of various kinds of hepatotoxic drugs in 3D ES/iPS-hepa.

2. Materials and methods

2.1. hESCs and hiPSCs culture

A hESC line, H1 and H9 (WiCell Research Institute), was maintained on a feeder layer of mitomycin C-treated mouse embryonic fibroblasts (Millipore) with Repro Stem medium (Repro CELL) supplemented with 5 ng/ml fibroblast growth factor 2 (FGF2) (Sigma). Both H1 and H9 were used following the Guidelines for Derivation and Utilization of Human Embryonic Stem Cells of the Ministry of Education, Culture, Sports, Science and Technology of Japan and furthermore, and the study was approved by Independent Ethics Committee.

Three human iPSC lines were provided from the JCRB Cell Bank (Tic, JCRB Number: JCRB1331; Dotcom, JCRB Number: JCRB1327; Toe, JCRB Number: JCRB1338) [14,15]. These human iPSC lines were maintained on a feeder layer of mitomycin C-treated mouse embryonic fibroblasts with iPSellon (Cardio) supplemented with 10 ng/ml FGF2. Other three human iPSC lines, 201B6, 201B7 and 253G1 were kindly provided by Dr. S. Yamanaka (Kyoto University) [2]. These human iPSC lines were maintained on a feeder layer of mitomycin C-treated mouse embryonic fibroblasts with Repro Stem supplemented with 5 ng/ml FGF2.

2.2. In vitro differentiation

Before the initiation of cellular differentiation, the medium of hESCs was exchanged into a defined serum-free medium, hESF9, and cultured as previously reported [16]. The differentiation protocol for the induction of definitive endoderm cells, hepatoblasts, and hepatocytes was based on our previous reports with some modifications [3–5,17]. Briefly, in mesendoderm differentiation, hESCs were dissociated into single cells by using Accutase (Millipore) and cultured for 2 days on Matrigel (BD Biosciences) in differentiation hESF-DIF medium which contains 100 ng/ml Activin A (R&D Systems) and 10 ng/ml bFGF (hESF-DIF medium was purchased from Cell Science & Technology Institute; differentiation hESF-DIF medium was supplemented with 10 μg/ml human recombinant insulin, 5 μg/ml human apotransferrin, 10 μM 2-mercaptoethanol, 10 μM ethanolamine, 10 μM sodium selenite, and 0.5 mg/ml bovine fatty acid free serum albumin [all from sigma]). To generate definitive endoderm cells, the mesendoderm cells were transduced with 3000 vector particle (VP)/cell of Ad-FOXA2 for 1.5 h on day 2 and cultured until day 6 on Matrigel in differentiation hESF-DIF medium supplemented with 100 ng/ml Activin A and 10 ng/ml bFGF. For induction of hepatoblasts, the DE cells were transduced with each 1500 VP/cell of Ad-FOXA2 and Ad-HNF1α for 1.5 h on day 6 and cultured for 3 days on Matrigel in hepatocyte culture medium (HCM) (Lonza) supplemented with 30 ng/ml bone morphogenetic protein 4 (BMP4) (R&D Systems) and 20 ng/ml FGF4 (R&D Systems). In hepatic expansion, the hepatoblasts were transduced with each 1500 VP/cell of Ad-FOXA2 and Ad-HNF1α for 1.5 h on day 9 and cultured for 3 days on Matrigel in HCM supplemented with 10 ng/ml hepatocyte growth factor (HGF), 10 ng/ml FGF1, 10 ng/ml FGF4, and 10 ng/ml FGF10 (all from R&D Systems). To perform hepatocyte maturation on Nanopillar Plate (a prototype multi-well culturing plate for spheroid culture developed and prepared by Hitachi High-Technologies Corporation) shown in Fig. 1B, the cells were seeded at 2.5×10^5 cells/cm^2 (Fig. S1) in hepatocyte culture medium (Fig. S2) supplemented with 10 ng/ml HGF, 10 ng/ml FGF1, 10 ng/ml FGF4, and 10 ng/ml FGF10 on day 11. In the first stage of hepatocyte maturation (from day 12 to day 25), the cells were cultured for 13 days on Matrigel in HCM supplemented with 20 ng/ml HGF, 20 ng/ml oncostatin M (OsM), 10 ng/ml FGF4, and 10^{-6} M dexamethasone (DEX). In the second stage of hepatocyte maturation (from day 25 to day 35), Matrigel was overlaid on the hepatocyte-like cells. Matrigel were diluted to a final concentration of 0.25 mg/ml with William's E medium (Invitrogen) containing 4 mM L-glutamine, 50 ug/ml gentamycin sulfate, 1 × ITS (BD Biosciences), 20 ng/ml OsM, and 10^{-6} M DEX. The culture medium was aspirated, and then the Matrigel solution (described above) was overlaid on the hepatocyte-like cells. The cells were incubated overnight, and the medium was replaced with HCM supplemented with 20 ng/ml OsM and 10^{-6} M DEX.

2.3. Adenovirus (Ad) vectors

Ad vectors were constructed by an improved *in vitro* ligation method [18,19]. The human EF-1α promoter-driven LacZ-, FOXA2-, or HNF1α-expressing Ad vectors (Ad-LacZ, Ad-FOXA2, or Ad-HNF1α, respectively) were constructed previously [3,4,20]. All of Ad vectors contain a stretch of lysine residue (K7) peptides in the C-terminal region of the fiber knob for more efficient transduction of hESCs, hiPSCs, and DE cells, in which transfection efficiency was almost 100%, and purified as described previously [3–5]. The vector particle (VP) titer was determined by using a spectrophotometric method [21].

2.4. Flow cytometry

Single-cell suspensions of hESC/hiPSC-derived cells were fixed with 2% paraformaldehyde (PFA) at 4°C for 20 min, and then incubated with the primary antibody (described in Table S1), followed by the secondary antibody (described in Table S1). Flow cytometry analysis was performed using a FACS LSR Fortessa flow cytometer (BD Biosciences).

2.5. RNA isolation and reverse transcription-polymerase chain reaction (RT-PCR)

Total RNA was isolated from hESCs or hiPSCs and their derivatives using ISOGENE (Nippon Gene). cDNA was synthesized using 500 ng of total RNA with a Superscript VILO cDNA synthesis kit (Invitrogen). Real-time RT-PCR was performed with Taqman gene expression assays (Applied Biosystems) or SYBR Premix Ex Taq (TaKaRa) using an ABI PRISM 7000 Sequence Detector (Applied Biosystems). Relative quantification was performed against a standard curve and the values were normalized against the input determined for the housekeeping gene, glyceraldehyde 3-phosphate dehydrogenase (GAPDH). The primer sequences used in this study are described in Table S2.

2.6. Immunohistochemistry

The cells were fixed with 4% PFA. After incubation with 1% Triton X-100, blocking with Blocking One (Nakalai tesque), the cells were incubated with primary antibody (describe in Table S1) at 4°C for over night, followed by incubation with a secondary antibody (described in Table S1) at room temperature for 1 h.

2.7. ELISA

The hESCs or hiPSCs were differentiated into hepatocytes as described in Fig. 1A. The culture supernatants, which were incubated for 24 h after fresh medium was added, were collected and analyzed for the amount of ALB secretion by ELISA. ELISA kits for ALB were purchased from Bethyl. ELISA was performed according to the manufacturer's instructions. The amount of ALB secretion was calculated according to each standard followed by normalization to the protein content per well.

2.8. Urea secretion

The hESCs or hiPSCs were differentiated into hepatocytes as described in Fig. 1A. The culture supernatants, which were incubated for 24 h after fresh medium was added, were collected and analyzed for the amount of urea secretion. Urea measurement kits were purchased from BioAssay Systems. The experiment was performed according to the manufacturer's instructions. The amount of urea secretion was calculated according to each standard followed by normalization to the protein content per well.

2.9. Canalicular secretory assay

At cellular differentiation, the hepatocyte-like cell spheroids were treated with 5 mM choly-lysyl-fluorescein (CLF) (BD Biosciences) for 30 min. The cells were washed with culture medium, and then observed by fluorescence microscope. To inhibit the function of BSEP, the cells were pretreated with Cyclosporin A 24 h before of the CLF treatment.

2.10. Assay for CYP activity and CYP induction

To measure the cytochrome P450 2C9 and 3A4 activity of the cells, we performed lytic assays by using a P450-GloTM CYP2C9 (catalog number; V8791) and

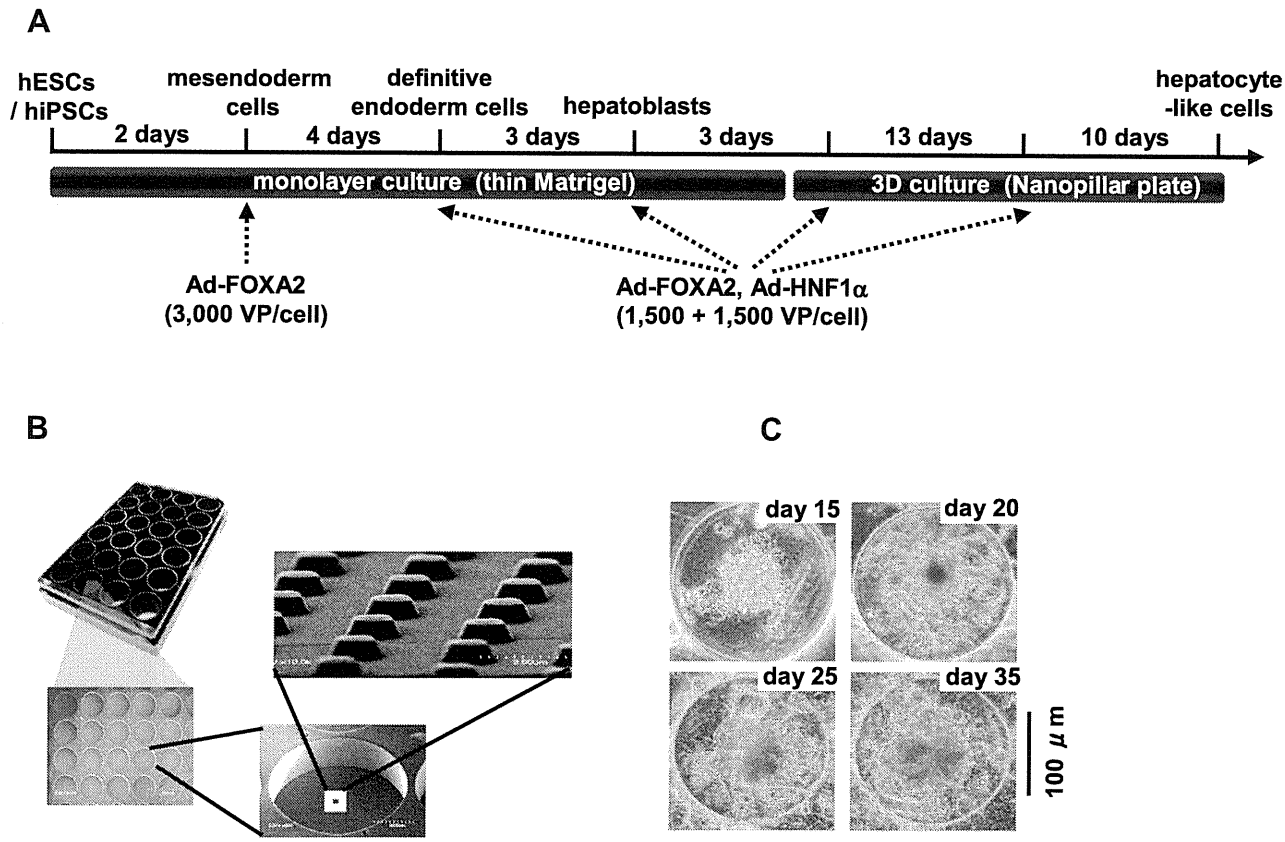

Fig. 1. Hepatocyte-like cells were differentiated from hESCs/hiPSCs by using Nanopillar Plate. (A) The procedure for differentiation of hESCs into 3D ES/iPS-hepa via mesendoderm cells, definitive endoderm cells, and hepatoblasts is presented schematically. In the differentiation, not only the addition of growth factors but also stage-specific transient transduction of both FOXA2- and HNF1α-expressing Ad vector (Ad-FOXA2 and Ad-HNF1α, respectively) was performed. The cellular differentiation procedure is described in detail in the materials and methods section. (B) Photograph display of a 24-well format Nanopillar Plate and its microstructural appearances of the hole and pillar structure. (C) Phase-contrast micrographs of the hESC-hepa spheroids on the Nanopillar Plate are shown. Scale bar represents 100 μm.

3A4 (catalog number; V9001) Assay Kit (Promega), respectively. We measured the fluorescence activity with a luminometer (Lumat LB 9507; Berthold) according to the manufacturer's instructions. The CYP activity was normalized with the protein content per well.

To measure CYP2C9 and 3A4 induction potency, the CYP activity was measured by using a P450-GloTM CYP2C9 and 3A4 Assay Kit, respectively. The cells were treated with rifampicin, which is known to induce both CYP2C9 and 3A4, at a final concentration of 10 μM for 48 h. The cells were also treated with Ketoconazole (Sigma) or Sulfaphenazole (Sigma), which are inhibitors for CYP3A4 or 2C9, at a final concentration of 1 μM or 2 μM, respectively, for 48 h. Controls were treated with DMSO (final concentration 0.1%). Inducer compounds were replaced daily.

2.11. Cell viability tests

Cell viability was assessed by the WST-8 assay kit (Dojindo) in Fig. 2D. After treatment with test compounds, such as Acetaminophen (Wako), Allopurinol (Wako), Amiodaron (Sigma), Benzbromarone (Sigma), Clozapine (Wako), Cyclizine (MP bio), Dantrolene (Wako), Desipramine (Wako), Disufliram (Wako), Erythromycin (Wako), Felbamate (Sigma), Flutamide (Wako), Isoniazid (Sigma), Labetalol (Sigma), Lefunomide (Sigma), Maprotiline (Sigma), Nefazodone (Sigma), Nitrofurantoin (Sigma), Sulindac (Wako), Tacrine (Sigma), Tebinafine (Wako), Tolcapone (TRC), Troglitazone (Wako), and Zafirlukast (Cayman) for 24 h, the cell viability was measured. The cell viability of the 3D iPSC-hepa were assessed by WST-8 assay after 24 h exposure to different concentrations of Aflatoxin B1 (Sigma) and Benzbromarone in the presence or absence of the CYP3A4 or 2C9 inhibitor, Ketoconazole (1 μM) or Sulfaphenazole (10 μM), respectively. The control refers to incubations in the absence of test compounds and was considered as 100% viability value. Controls were treated with DMSO (final concentration 0.1%). ATP assay (BioAssay Systems), Alamar Blue assay (Invitrogen), and Crystal Violet (Wako) staining assay were performed according to the manufacturer's instructions.

2.12. Primary human hepatocytes

Three lots of cryopreserved human hepatocytes (lot Hu8072 [CellzDirect], HC2-14, and HC10-101 [Xenotech]) were used. These three lots of crypreserved human hepatocytes were cultured according to our previous report [5].

2.13. Statistical analysis

Statistical analysis was performed using the unpaired two-tailed Student's *t*-test. All data are represented as means ± SD ($n = 3$).

3. Results

The 3D ES/iPS-hepa were generated from hESCs/hiPSCs as shown in Fig. 1A. Hepatocyte differentiation of hESCs/hiPSCs was efficiently promoted by stage-specific transient transduction of FOXA2 and HNF1α in addition to the treatment with appropriate soluble factors (growth factors and cytokines) [6]. On day 11, the hESC-derived cells were seeded at 2.5×10^5 cells/cm^2 (Fig. S1) on Nanopillar Plate (Fig. 1B), in hepatocyte culture medium (Fig. S2) to promote hepatocyte maturation. In addition, Matrigel was overlaid on the 3D ES-hepa to promote further hepatocyte maturation. The 3D ES-hepa with compact morphology that were adhesive to the substratum and had an optimal size (approximately 100 μm in diameter) were formed by using the Nanopillar Plate (Fig. 1C). The spheroids seem to be stable because they could be cultured for more than 20 days. We have confirmed that more than 90% of the cells that constitute the spheroids were alive, indicating that the necrotic centers are absent.

To investigate whether or not a 3D spheroid culture could promote hepatocyte maturation of the hepatocyte-like cells, various hepatocyte characteristics of the 3D ES/iPS-hepa were compared with those of the monolayer-cultured hESC- or hiPSC-derived hepatocyte-like cells (mono ES-hepa or mono iPS-hepa). The gene expression level of *ALB* peaked on day 20 in the mono ES-hepa, and then it was dramatically decreased after day 25 (Fig. 2A). In contrast, the gene expression level of *ALB* was

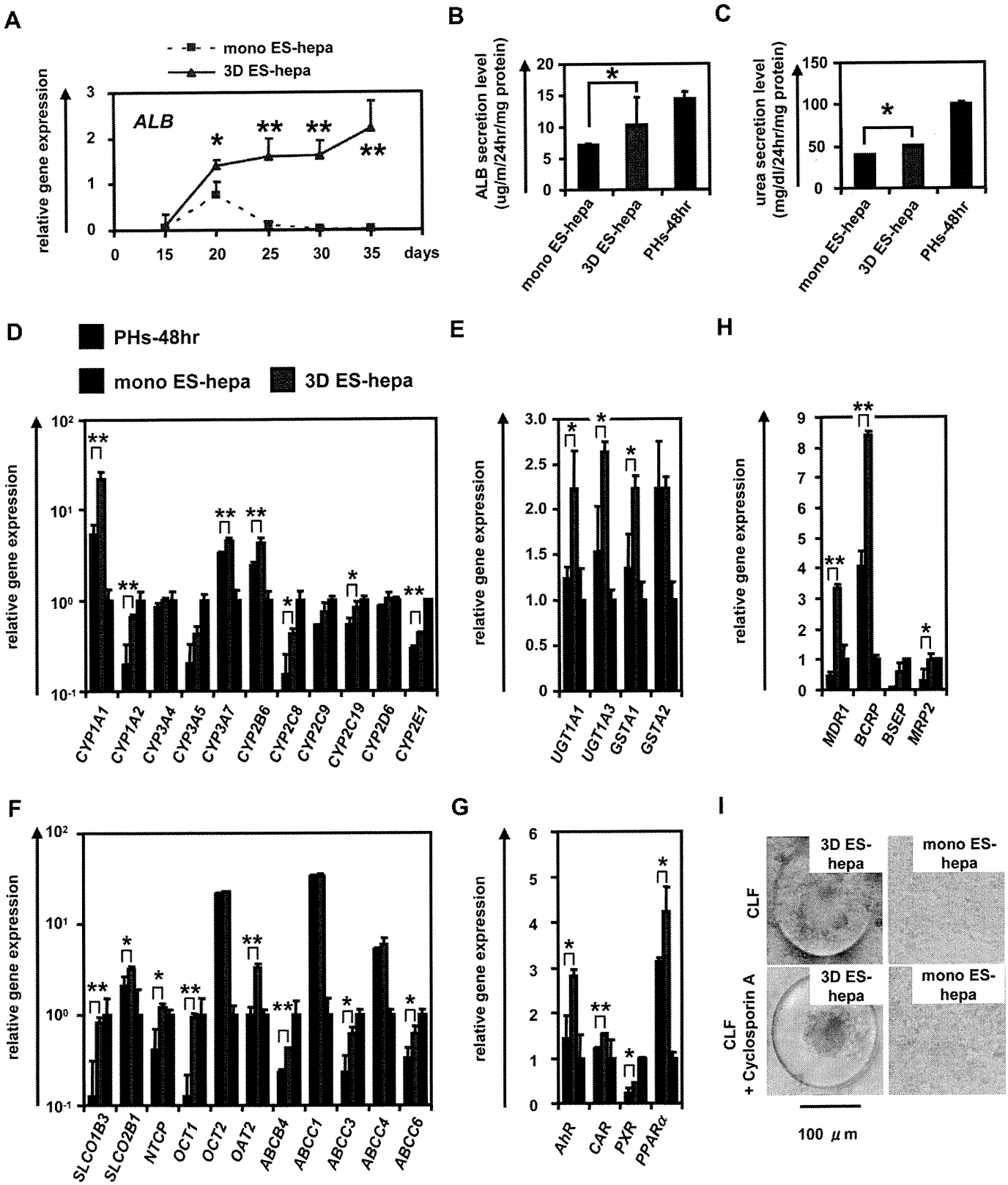

Fig. 2. Hepatocyte functions in hESC-derived hepatocyte-like cells were enhanced by using Nanopillar Plate. (A) The gene expression levels of *ALB* were measured by real-time RT-PCR on day 15, 20, 25, 30, and 35. On the *y* axis, the gene expression levels in PHs (three lots of PHs were used in all studies), which were cultured for 48 h after plating (PHs-48hr), were taken as 1.0. (B, C) The amount of ALB (B) and urea (C) secretion were examined in the mono ES-hepa (day 20), the 3D ES-hepa (day 35), and PHs-48hr. (D–H) The gene expression levels of CYP enzymes (D), conjugating enzymes (E), hepatic transporters (F), hepatic nuclear receptors (G), and bile canaliculi transporters (H) were examined by real-time RT-PCR in the mono ES-hepa, the 3D ES-hepa, and PHs-48hr. On the *y* axis, the expression levels in PHs-48hr were taken as 1.0. (I) The ability of bile acid uptake and efflux was examined in the mono ES-hepa and 3D ES-hepa. Choly-lysyl-fluorescein (CLF) (5 μM) was used for the observation of bile canaliculi uptake and efflux. To inhibit transportation by BSEP, the cells were pretreated with 1 μM Cyclosporin A. $^{*}P < 0.05$; $^{**}P < 0.01$.

moderately increased in the 3D ES-hepa until day 35 (Fig. 2A). These results suggest that the hepatocyte functions of the 3D ES-hepa are sustained for more than 2 weeks on the Nanopillar Plate, although those of the mono ES-hepa are rapidly devitalized (Fig. 2A and Fig. S4). Other hepatocyte characteristics, such as ability of ALB and urea secretion and gene expression levels of hepatocyte-related markers in the 3D ES-hepa were compared with those of the mono ES-hepa (Fig. 2B–H). Because the gene expression level of *ALB* in the 3D ES-hepa was the highest on day 35 and that in mono ES-hepa was the highest on day 20, various hepatocyte characteristics were compared on day 35 or day 20, respectively. The amount of ALB (Fig. 2B) and urea (Fig. 2C) secretion in the 3D ES-hepa was higher than those of the mono ES-hepa. The gene expression levels of CYP enzymes (Fig. 2D), conjugating enzymes (Fig. 2E), hepatic transporters (Fig. 2F), hepatic nuclear receptors (Fig. 2G), and hepatic transcription factors (Fig. S5) in the 3D ES-hepa were higher than those in the mono ES-hepa. The expression levels of most of the genes in the 3D ES-hepa were higher than those in the mono ES-hepa. Because the previous study [11] showed that hepatocyte spheroids expressed hepatocyte transporters similar to those of the bile canaliculi in native liver tissue, the gene expression levels of bile canaliculi transporters (Fig. 2H), as well as the ability of bile acid uptake and efflux, (Fig. 2I) were examined in the 3D ES-hepa. The gene expression levels of bile canaliculi transporters were increased in the 3D ES-hepa compared with those of mono ES-hepa and PHs (Fig. 2H). The bile canaliculi formation was visualized by BSEP fluorescent substrate: Cholyl-lysyl-fluorescein (CLF), which is inhibited by BSEP

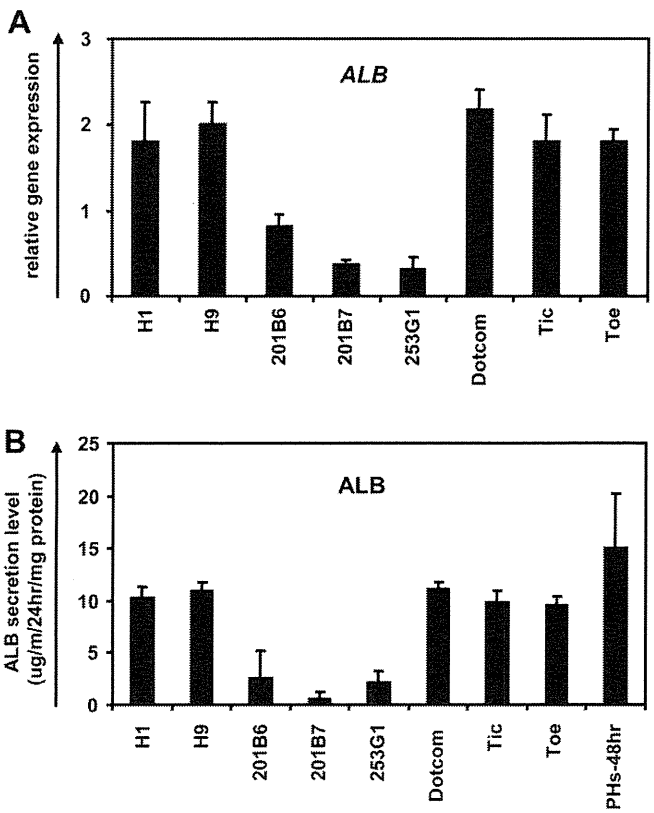

Fig. 3. Comparison of the hepatic differentiation capacities of various hESC and hiPSC lines hESCs (H1 and H9) and hiPSCs (201B6, 201B7, 253G1, Dotcom, Tic, and Toe) were differentiated into the 3D ES/iPS-hepa as described in Fig. 1A. (A) On day 20, the gene expression level of *ALB* was examined by real-time RT-PCR. On the *y* axis, the gene expression level of *ALB* in PHs-48hr was taken as 1.0. (B) On day 20, the amount of ALB secretion was examined by ELISA. The amount of ALB secretion was calculated according to each standard followed by normalization to the protein content per well.

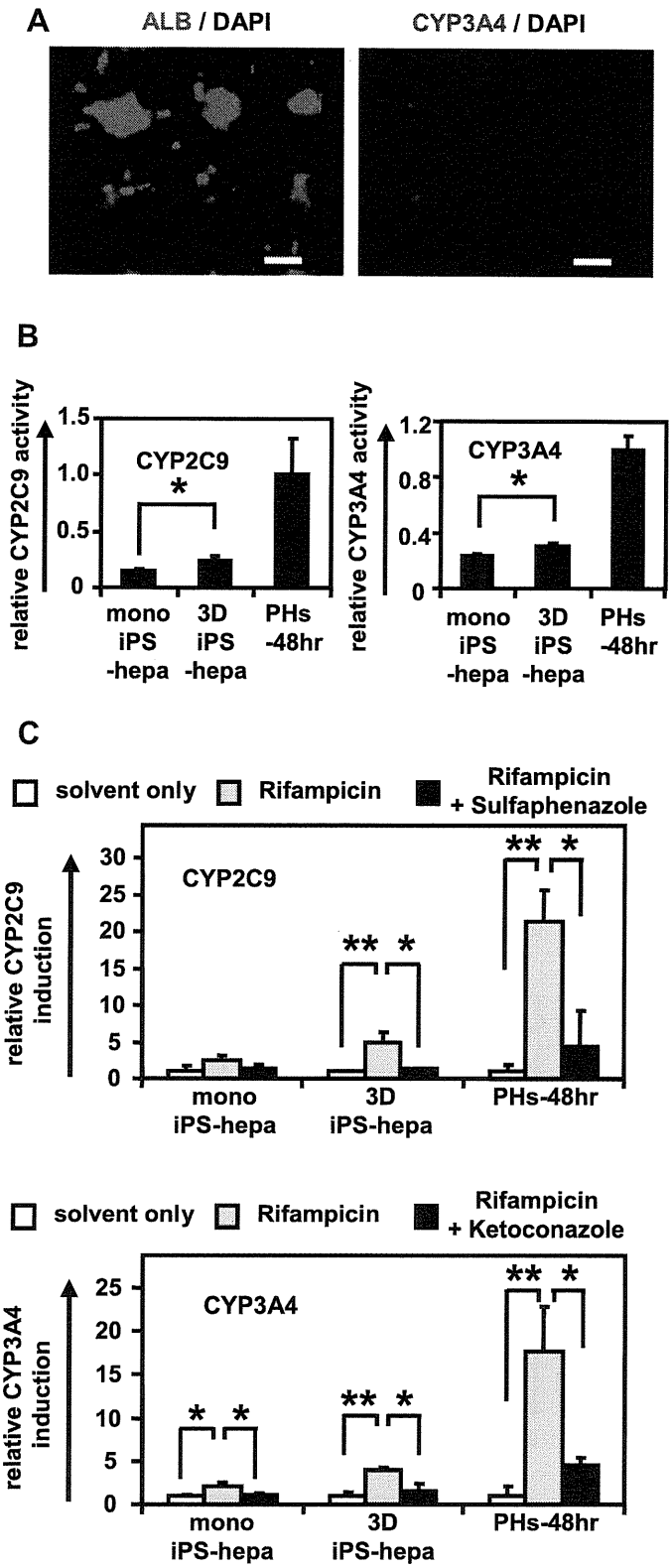

Fig. 4. Drug metabolism capacity and CYP induction potency were examined in the 3D iPS-hepa. (A) The 3D iPS-hepa (day 35) were subjected to immunostaining with anti-ALB (green) or CYP3A4 (red) antibodies. Nuclei were counterstained with DAPI (blue). Scale bar represents 100 μm. (B) The CYP activity was measured in the mono iPS-hepa (day 20), the 3D iPS-hepa (day 35), and PHs-48hr. On the *y* axis, the CYP activity in PHs-48hr was taken as 1.0. (C) Induction of CYP2C9 (left) or CYP3A4 (right) by DMSO (solvent only; white bar), Rifampicin (gray bar), or rifampicin and CYP inhibitor (Sulfaphenazole or Ketoconazole, black bar) in the mono iPS-hepa, the 3D iPS-hepa, and PHs-48hr. On the *y* axis, the CYP activity of the cells that have been cultured in DMSO-containing medium was taken as 1.0. $^{*}P < 0.05$; $^{**}P < 0.01$.

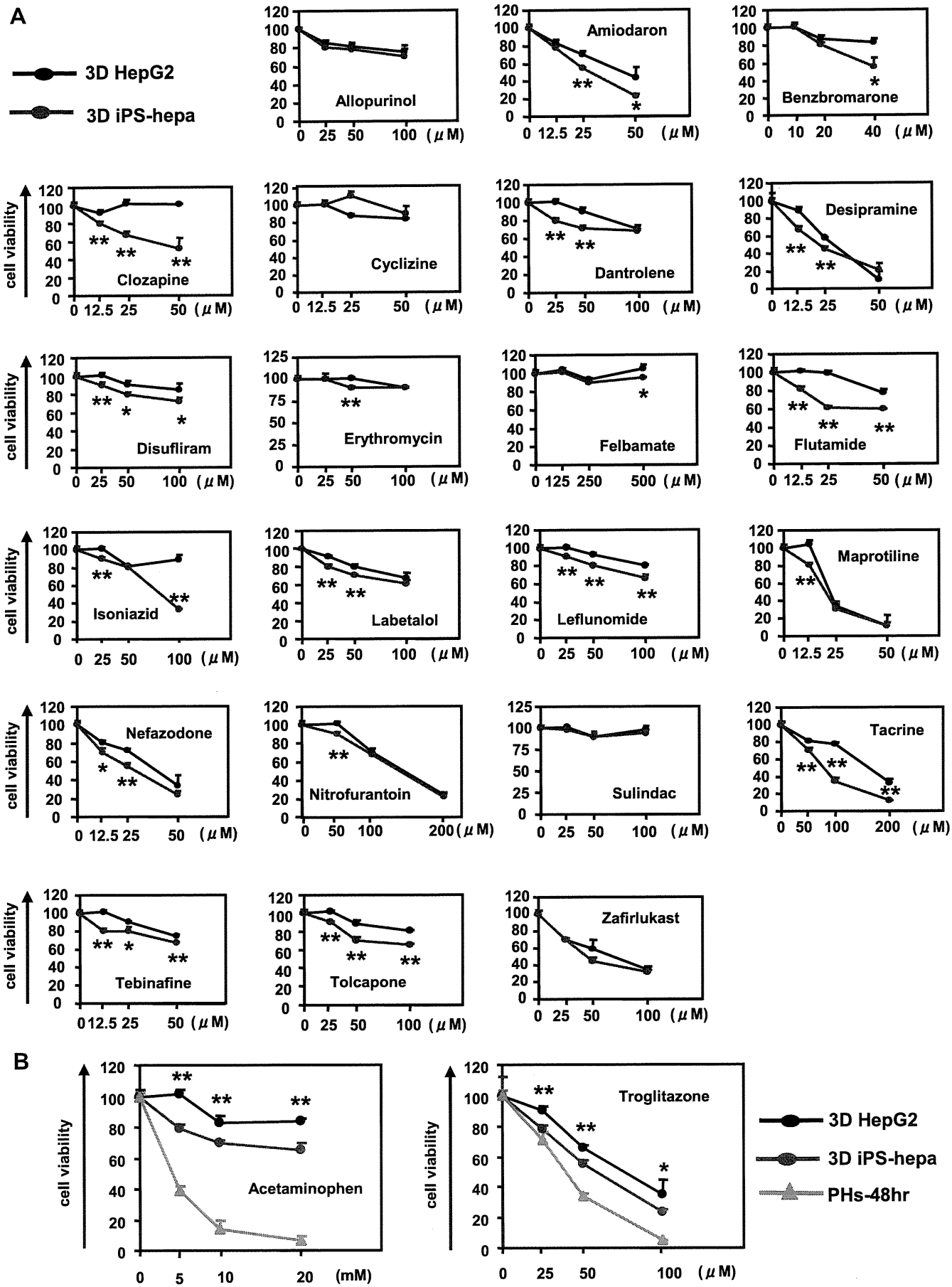
A
3D HepG2
3D iPS-hepa
cell viability
Allopurinol
Amiodaron
Benzbromarone
Clozapine
Cyclizine
Dantrolene
Desipramine
Disufliram
Erythromycin
Felbamate
Flutamide
Isoniazid
Labetalol
Leflunomide
Maprotiline
Nefazodone
Nitrofurantoin
Sulindac
Tacrine
Tebinafine
Tolcapone
Zafirlukast
B
Acetaminophen
Troglitazone
3D HepG2
3D iPS-hepa
PHs-48hr
(μM)
(mM)

inhibitor Cyclosporin A [22,23]. More CLF was accumulated in the 3D ES-hepa than in the mono ES-hepa (Fig. 2I *upper panel*). Moreover, CLF accumulation was inhibited by Cyclosporin A treatment only in the 3D ES-hepa (Fig. 2I *lower panel*), demonstrating that the functionality of BSEP transporter in 3D ES-hepa was greater than that in mono ES-hepa. These results suggested that hepatocyte maturation was promoted by the culture on the Nanopillar Plate. It is likely that, compared to the monolayer culture condition, the 3D spheroid-culture condition is more similar to the *in vivo* condition.

It is important to select an hESC/hiPSC line that has a strong ability to differentiate into hepatocyte-like cells in the case of medical applications such as drug screening. In this study, two hESC lines and six hiPSC lines were differentiated into the hepatocyte-like cells, and then their gene expression levels of *ALB* (Fig. 3A) and ALB secretion levels (Fig. 3B) were compared. These results suggest that the iPSC line, Dotcom, was the suitable cell line for hepatocyte maturation. Therefore, the iPSC line, Dotcom, was used to examine the possibility of the 3D iPS-hepa for drug screening. The drug metabolism capacity and the CYP induction potency of the 3D iPS-hepa were compared with those of the mono iPS-hepa. We confirmed the expression of ALB and CYP3A4 protein in the 3D ES-hepa (Fig. 4A). The activity levels of CYP enzymes in the 3D iPS-hepa were measured according to the metabolism of the CYP2C9 or CYP3A4 substrates (Fig. 4B); the levels were higher than those of the mono iPS-hepa (Fig. 4B). We further tested the induction of CYP2C9 and CYP3A4 by chemical stimulation (rifampicin was used as a CYP2C9 or CYP3A4 inducer). Compared with mono iPS-hepa, the 3D iPS-hepa produced more metabolites in response to chemical stimulation (Fig. 4C). In addition, the CYP induction was inhibited by using CYP2C9 or CYP3A4 inhibitor (Sulfaphenazole or Ketoconazole, respectively). These results indicated that drug metabolism capacity and CYP induction potency in 3D iPS-hepa were higher than those in mono iPS-hepa.

Many researchers have tried to predict the drug-induced cytotoxicity *in vitro* using hepatocarcinoma-derived cells such as HepG2 cells [24,25]. HepG2 cells are less expensive than PHs and the reproducible experiments are easier to perform than they are with PHs, although 30% of the compounds were incorrectly classified as nontoxic [24,25]. To overcome these problems, hESC/hiPSC-derived hepatocyte-like cells are expected to be used to predict drug-induced cytotoxicity. To examine its applicability to drug screening, the 3D iPS-hepa were treated with various drugs, that cause hepatotoxicity. WST-8 assay was performed to evaluate cell viability (Fig. S6). The susceptibility of the 3D iPS-hepa to most of the hepatotoxic drugs was higher than that of the mono iPS-hepa (Fig. S7). Compared to the mono iPS-hepa, the 3D iPS-hepa were more suitable tools for drug screening. Next, the susceptibility of the 3D iPS-hepa to the hepatotoxic drugs was compared with that of the 3D spheroid cultured HepG2 cells (3D HepG2; the hepatocyte functions of 3D HepG2 cells are higher than those of monolayer cultured HepG2 cells [Fig. S8]). With most of the drugs, the cell viability of the 3D iPS-hepa was lower than that of the 3D HepG2 (Fig. 5A). These results indicated that the 3D iPS-hepa are more valuable tools for drug screening than the 3D HepG2. However, the susceptibility of the 3D iPS-hepa to Acetaminophen and Troglitazone was lower than that of the PHs which were cultured for 48 h after the cells were plated (Fig. 5B). These results might be due to the lower activity levels of CYPs in 3D iPS-hepa as compared as those in PHs. Taken together, 3D iPS-hepa are more valuable tools for drug screening than the 3D HepG2, although further maturation of 3D iPS-hepa is still required for 3D iPS-hepa to be an alternative cell source of PHs in the drug screening.

To examine whether drug-induced cytotoxicity is caused by CYP metabolites in 3D iPS-hepa, Aflatoxin B1 (mainly metabolized by CYP3A4 [26]) and Benzbromarone (mainly metabolized by CYP2C9 [27]) were treated in the presence or absence of a CYP3A4 and a 2C9 inhibitor, Ketoconazole and Sulfaphenazole, respectively (Fig. 6). The cell viability of 3D iPS-hepa was partially rescued by treatment with the CYP inhibitor. These results indicated that drug-induced cytotoxicity was caused by CYP metabolites of Aflatoxin B1 and Benzbromarone.

4. Discussion

Recently, it has been expected that human pluripotent stem cells and their derivatives, including hepatocyte-like cells, will be utilized in applications for the safety assessment of drugs. We have previously reported that combinational overexpression of SOX17, HEX, and HNF4α, or combinational overexpression of FOXA2 and HNF1α could promote hepatocyte differentiation [5,6]. However, the drug metabolism capacity of the hepatocyte-like cells generated by our previous protocol was still lower than that of primary human hepatocytes [6]. To generate more matured hepatocyte-like cells as compared with our previous protocol, we established a hepatocyte differentiation method employing not only stage-specific transient overexpression of hepatocyte-related transcription factors but also a 3D culture systems using a Nanopillar Plate, was established. Although the use of hepatocyte-like cells generated from hESCs/hiPSCs in application for drug toxicity testing has begun to be focused, to the best of our knowledge, there have been few studies that have investigated whether hepatocyte-like cells could predict many kinds of drug-induced toxicity.

3D culture spheroids were generated from hESCs/hiPSCs by using a Nanopillar Plate. The diameter of the spheroids was approximately 100 μm on day 35 of differentiation (Fig. 1C). Because it is known that the no-oxygen limitation would take place in spheroids up to 100 μm in diameter [28], the size of the spheroid might be important to generate spheroids with high viability. A Nanopillar Plate has a potential to regulate the spheroid diameter simply by culturing under optimized seeding condition, on its suitably designed pillar and hole structure [11]. Therefore, a Nanopillar Plate would be a suitable environment for the generation of 3D ES/iPS-hepa that show high viability and possess high level of hepatocellular functions.

The levels of many hepatocyte functions, such as ALB secretion ability (Fig. 2B), urea secretion ability (Fig. 2C), hepatocyte-related gene expressions (Fig. 2D–H), drug metabolism capacity (Fig. 4B), and CYP induction potency (Fig. 4C), of 3D ES/iPS-hepa were higher than those of mono ES/iPS-hepa. This might have been because the structural and functional polarity, which can be seen in the naïve environment of hepatocytes, of the hepatocyte-like cells was configured by a 3D culturing condition. Previous studies have shown that a 3D culture condition is suitable to maintain the hepatic characteristics of the isolated hepatocytes because this condition mimic *in vivo* environment [29,30]. These facts indicated that the 3D culture condition is a more suitable condition for the hepatocyte-like cells than the monolayer culture condition.

Two hES cell lines and six hiPS cell lines were differentiated into the hepatocyte-like cells in this study. The hiPS cell line, Dotcom, seemed to be a suitable cell line for hepatic differentiation (Fig. 3). Because the hepatic differentiation propensity differs among the

Fig. 5. The possibility of applying 3D iPS-hepa to drug testing was examined. (A) The cell viability of the 3D HepG2 (black) and 3D iPSC-hepa (red) were assessed by WST-8 assay after 24 h exposure to different concentrations of 22 test compounds. (B) The cell viability of the 3D HepG2 (black), 3D iPSC-hepa (red), and PHs-48hr (green) were assessed by WST-8 assay after 24 h exposure to different concentrations of Acetaminophen and Troglitazone. Cell viability is expressed as a percentage of cells treated with solvent only. $^{*}P < 0.05$; $^{**}P < 0.01$.

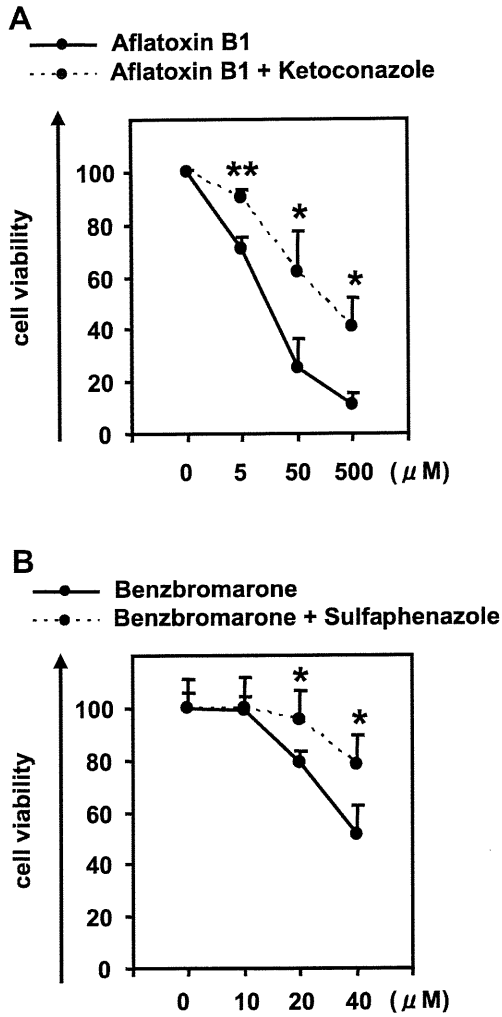

Fig. 6. Drug-induced cytotoxicity in the 3D iPS-hepa is mediated by cytochrome P450. (A, B) The cell viability of the 3D iPSC-hepa was assessed by WST-8 assay after 24 h exposure to different concentrations of (A) Aflatoxin B1 and (B) Benzbromarone in the presence or absence of the CYP3A4 or 2C9 inhibitor, Ketoconazole or Sulfaphenazole, respectively. Cell viability was expressed as the percentage of cells treated with solvent only. $^{*}P < 0.05$; $^{**}P < 0.01$.

hES/hiPS cell lines, it would be important to select an appropriate cell line for medical applications such as drug screening. However, the dominant reason for this hepatic differentiation propensity is not been well known. It would be interesting study to elucidate the mechanism of this propensity.

Although the drug metabolism capacity and CYP induction potency of 3D iPS-hepa were higher than those of mono iPS-hepa (Fig. 4B and C), they were still lower than those of primary human hepatocytes. The hepatic nuclear factors are known to be key molecules in the CYP induction of hepatocytes [30]. Therefore, overexpression of hepatic nuclear factors, which are not abundantly expressed in the hepatocyte-like cells (such as *PXR*), might upregulate the CYP induction potency of the hepatocyte-like cells.

3D iPS-hepa were more sensitive for detection of the drug-induced cytotoxicity than HepG2 cells that are widely used to predict hepatotoxicity [31,32] (Fig. 5). In addition, the decrease of cell viability, which was caused by hepatotoxic drugs, of 3D iPS-hepa was partially rescued by treatment with a CYP inhibitor (Fig. 6). These data suggest that the hepatocyte-like cells could detect the toxicity of the reactive metabolites that were generated by drug metabolizing enzymes such as CYP enzymes. Because in many cases, drug-induced hepatotoxicity is caused by the reactive metabolites produced by drug metabolizing enzymes [33], our finding that the hepatocyte-like cells could detect the toxicity of reactive metabolites should be of great potential for toxicological screening. Moreover, it might be possible to predict idiosyncratic liver toxicity by using hepatocyte-like cells generated from hiPSCs that were established from a patient with a rare CYP polymorphism. However, some compounds did not show any cytotoxicity (such as Cyclizine, Felbamate, and Sulindac) (Fig. 5). To apply the hepatocyte-like cells for wide-spread drug screening, generation of the hepatocyte-like cells are required to detect hepatotoxity in more sensitive manner. Previous studies showed that the depletion of conjugating enzymes [32] or knockdown of Nrf2 [34] expression are useful to upregulate the sensitivity to hepatotoxic drugs. Therefore, these approaches would be useful to generate more sensitive hepatocytes to toxic drugs.

5. Conclusions

In this study, we established the efficient hepatocyte differentiation method which employs not only stage-specific transient overexpression of hepatocyte-related transcription factors but also 3D spheroid culture systems by using Nanopillar Plate. To the best of our knowledge, this is the first study in which the hepatocyte-like cells, having enough hepatocyte functions, mediate drug-induced cytotoxicity against many compounds. Our hepatocyte-like cells differentiated from hESCs or hiPSCs have potential to be applied in drug toxicity testing.

Acknowledgments

We thank Misae Nishijima and Hiroko Matsumura for their excellent technical support. HM, KK, MKF, and TH were supported by grants from the Ministry of Health, Labor, and Welfare of Japan. HM was also supported by Japan Research foundation For Clinical Pharmacology, and The Uehara Memorial Foundation. MKF was also supported by Japan Society for the Promotion of Science Grant-in-Aid for Scientific Research. FS was supported by Program for Promotion of Fundamental Studies in Health Sciences of the National Institute of Biomedical Innovation (NIBIO). We thank Hiromu Yamada (NIBIO) for helpful discussion.

Appendix A. Supplementary data

Supplementary data related to this article can be found at http://dx.doi.org/10.1016/j.biomaterials.2012.11.029.

References

[1] Thomson JA, Itskovitz-Eldor J, Shapiro SS, Waknitz MA, Swiergiel JJ, Marshall VS, et al. Embryonic stem cell lines derived from human blastocysts. Science 1998;282:1145–7.
[2] Takahashi K, Tanabe K, Ohnuki M, Narita M, Ichisaka T, Tomoda K, et al. Induction of pluripotent stem cells from adult human fibroblasts by defined factors. Cell 2007;131:861–72.
[3] Inamura M, Kawabata K, Takayama K, Tashiro K, Sakurai F, Katayama K, et al. Efficient generation of hepatoblasts from human ES cells and iPS cells by transient overexpression of homeobox gene HEX. Mol Ther 2011;19:400–7.
[4] Takayama K, Inamura M, Kawabata K, Tashiro K, Katayama K, Sakurai F, et al. Efficient and directive generation of two distinct endoderm lineages from human ESCs and iPSCs by differentiation stage-specific SOX17 transduction. PLoS One 2011;6:e21780.
[5] Takayama K, Inamura M, Kawabata K, Katayama K, Higuchi M, Tashiro K, et al. Efficient generation of functional hepatocytes from human embryonic stem cells and induced pluripotent stem cells by HNF4alpha transduction. Mol Ther 2012;20:127–37.
[6] Takayama K, Inamura M, Kawabata K, Sugawara M, Kikuchi K, Higuchi M, et al. Generation of metabolically functioning hepatocytes from human pluripotent stem cells by FOXA2 and HNF1alpha transduction. J Hepatol 2012;57:628–36.
[7] Ramasamy TS, Yu JS, Selden C, Hodgson H, Cui W. Application of three-dimensional culture conditions to human embryonic stem cell-derived

definitive endoderm cells enhances hepatocyte differentiation and functionality. Tissue Eng Part A. http://dx.doi.org/10.1089/ten.tea.2012.0190. Available from URL: http://www.ncbi.nlm.nih.gov/pubmed/23003670; 2012.
[8] Nagamoto Y, Tashiro K, Takayama K, Ohashi K, Kawabata K, Sakurai F, et al. The promotion of hepatic maturation of human pluripotent stem cells in 3D co-culture using type I collagen and Swiss 3T3 cell sheets. Biomaterials 2012;33:4526–34.
[9] Meng Q, Haque A, Hexig B, Akaike T. The differentiation and isolation of mouse embryonic stem cells toward hepatocytes using galactose-carrying substrata. Biomaterials 2012;33:1414–27.
[10] Shiraki N, Yamazoe T, Qin Z, Ohgomori K, Mochitate K, Kume K, et al. Efficient differentiation of embryonic stem cells into hepatic cells in vitro using a feeder-free basement membrane substratum. PLoS One 2011;6:e24228.
[11] Takahashi R, Sonoda H, Tabata Y, Hisada A. Formation of hepatocyte spheroids with structural polarity and functional bile canaliculi using nanopillar sheets. Tissue Eng Part A 2010;16:1983–95.
[12] Tong JZ, Sarrazin S, Cassio D, Gauthier F, Alvarez F. Application of spheroid culture to human hepatocytes and maintenance of their differentiation. Biol Cell 1994;81:77–81.
[13] Bi YA, Kazolias D, Duignan DB. Use of cryopreserved human hepatocytes in sandwich culture to measure hepatobiliary transport. Drug Metab Dispos 2006;34:1658–65.
[14] Makino H, Toyoda M, Matsumoto K, Saito H, Nishino K, Fukawatase Y, et al. Mesenchymal to embryonic incomplete transition of human cells by chimeric OCT4/3 (POU5F1) with physiological co-activator EWS. Exp Cell Res 2009;315:2727–40.
[15] Nagata S, Toyoda M, Yamaguchi S, Hirano K, Makino H, Nishino K, et al. Efficient reprogramming of human and mouse primary extra-embryonic cells to pluripotent stem cells. Genes Cells 2009;14:1395–404.
[16] Furue MK, Na J, Jackson JP, Okamoto T, Jones M, Baker D, et al. Heparin promotes the growth of human embryonic stem cells in a defined serum-free medium. Proc Natl Acad Sci U S A 2008;105:13409–14.
[17] Kawabata K, Inamura M, Mizuguchi H. Efficient hepatic differentiation from human iPS cells by gene transfer. Methods Mol Biol 2012;826:115–24.
[18] Mizuguchi H, Kay MA. Efficient construction of a recombinant adenovirus vector by an improved in vitro ligation method. Hum Gene Ther 1998;9:2577–83.
[19] Mizuguchi H, Kay MA. A simple method for constructing E1- and E1/E4-deleted recombinant adenoviral vectors. Hum Gene Ther 1999;10:2013–7.
[20] Tashiro K, Kawabata K, Sakurai H, Kurachi S, Sakurai F, Yamanishi K, et al. Efficient adenovirus vector-mediated PPAR gamma gene transfer into mouse embryoid bodies promotes adipocyte differentiation. J Gene Med 2008;10:498–507.
[21] Maizel Jr JV, White DO, Scharff MD. The polypeptides of adenovirus. I. Evidence for multiple protein components in the virion and a comparison of types 2, 7A, and 12. Virology 1968;36:115–25.
[22] Yasumiba S, Tazuma S, Ochi H, Chayama K, Kajiyama G. Cyclosporin A reduces canalicular membrane fluidity and regulates transporter function in rats. Biochem J 2001;354:591–6.
[23] Roman ID, Fernandez-Moreno MD, Fueyo JA, Roma MG, Coleman R. Cyclosporin A induced internalization of the bile salt export pump in isolated rat hepatocyte couplets. Toxicol Sci 2003;71:276–81.
[24] Rodriguez-Antona C, Donato MT, Boobis A, Edwards RJ, Watts PS, Castell JV, et al. Cytochrome P450 expression in human hepatocytes and hepatoma cell lines: molecular mechanisms that determine lower expression in cultured cells. Xenobiotica 2002;32:505–20.
[25] Hewitt NJ, Hewitt P. Phase I and II enzyme characterization of two sources of HepG2 cell lines. Xenobiotica 2004;34:243–56.
[26] Gallagher EP, Kunze KL, Stapleton PL, Eaton DL. The kinetics of aflatoxin B1 oxidation by human cDNA-expressed and human liver microsomal cytochromes P450 1A2 and 3A4. Toxicol Appl Pharmacol 1996;141:595–606.
[27] Lee MH, Graham GG, Williams KM, Day RO. A benefit-risk assessment of benzbromarone in the treatment of gout. Was its withdrawal from the market in the best interest of patients? Drug Saf 2008;31:643–65.
[28] Glicklis R, Merchuk JC, Cohen S. Modeling mass transfer in hepatocyte spheroids via cell viability, spheroid size, and hepatocellular functions. Biotechnol Bioeng 2004;86:672–80.
[29] Kim K, Ohashi K, Utoh R, Kano K, Okano T. Preserved liver-specific functions of hepatocytes in 3D co-culture with endothelial cell sheets. Biomaterials 2012;33:1406–13.
[30] Khetani SR, Bhatia SN. Microscale culture of human liver cells for drug development. Nat Biotechnol 2008;26:120–6.
[31] Iwamura A, Fukami T, Hosomi H, Nakajima M, Yokoi T. CYP2C9-mediated metabolic activation of losartan detected by a highly sensitive cell-based screening assay. Drug Metab Dispos 2011;39:838–46.
[32] Hosomi H, Akai S, Minami K, Yoshikawa Y, Fukami T, Nakajima M, et al. An in vitro drug-induced hepatotoxicity screening system using CYP3A4-expressing and gamma-glutamylcysteine synthetase knockdown cells. Toxicol In Vitro 2010;24:1032–8.
[33] Guengerich FP, MacDonald JS. Applying mechanisms of chemical toxicity to predict drug safety. Chem Res Toxicol 2007;20:344–69.
[34] Hosomi H, Fukami T, Iwamura A, Nakajima M, Yokoi T. Development of a highly sensitive cytotoxicity assay system for CYP3A4-mediated metabolic activation. Drug Metab Dispos 2011;39:1388–95.

Knee Surg Sports Traumatol Arthrosc (2012) 20:95–101
DOI 10.1007/s00167-011-1551-8

KNEE

Triple-bundle ACL grafts evaluated by second-look arthroscopy

Yoshinari Tanaka · Konsei Shino · Shuji Horibe · Norimasa Nakamura · Shigeto Nakagawa · Tatsuo Mae · Hidenori Otsubo · Tomoyuki Suzuki · Ken Nakata

Received: 13 February 2011 / Accepted: 10 May 2011 / Published online: 24 May 2011

Abstract
Purpose The purpose of this study was to evaluate the morphology of transplanted triple-bundle anterior cruciate ligament (ACL) grafts by second-look arthroscopy.
Methods The subjects were 41 patients with a mean age of 25.5 ± 8.5 years who underwent second-look arthroscopy at between 6 and 22 months after the anatomical triple-bundle ACL reconstruction using semitendinosus tendon autograft. Lachman test was negative in 38 knees and mildly positive with a firm endpoint in 3 knees. Arthroscopic evaluation of grafts was performed for the anteromedial graft (AM), the intermediate graft (IM), and the posterolateral graft (PL), focusing on tension and graft damage.
Results All grafts showed "fan-out" shape approaching the tibial attachment, which looked closer to the natural ACL compared to the double-bundle grafts. As to graft tension, 93% of AM, 90% of IM, and 88% of PL grafts were evaluated as taut, respectively. As to graft damage, there was no apparent rupture in the AM and IM grafts, while complete or substantial rupture was observed in 10% of PL grafts around the femoral tunnel aperture. The incidence of graft rupture in PL grafts was significantly greater than those in the AM and IM grafts. As to synovial coverage, 76% of AM, 78% of IM, and 59% of PL grafts were evaluated as "Good," while 41% of PL grafts were not fully covered with synovium. All of the synovial defects were observed around the femoral tunnel aperture.
Conclusion The morphology of the triple-bundle grafts resembled that of the natural ACL, while complete or substantial rupture was observed in 10% of the PL grafts.
Level of evidence Study of case series with no comparison group, Level IV.

Keywords Triple-bundle ACL reconstruction · Semitendinosus tendon autograft · Second-look arthroscopy · Graft morphology

Y. Tanaka (✉) · S. Horibe
Department of Sports Orthopaedics, Osaka Rosai Hospital, 1179-3 Nagasone-cho, Kita-ku, Sakai, Osaka 583-8555, Japan
e-mail: yoshi-tanaka@iris.eonet.ne.jp

K. Shino
Faculty of Comprehensive Rehabilitation, Osaka Prefecture University, Sakai, Japan

N. Nakamura
Institute for Medical Science in Sports, Osaka Health Science University, Kumatori, Japan

S. Nakagawa
Department of Sports Orthopaedics, Yukioka Hospital, Osaka, Japan

H. Otsubo · T. Suzuki
Department of Orthopaedics, Sapporo Medical University, Sapporo, Japan

T. Mae · K. Nakata
Department of Orthopaedic Surgery, Osaka University Graduate School of Medicine, Osaka University, Osaka, Japan

Introduction

Anterior cruciate ligament (ACL) reconstruction using hamstring tendon has become popular because of less donor site morbidity [4, 6, 14]. In addition, recent improvement in operative technique has made it possible to perform anatomical double-bundle ACL reconstruction, superior in biomechanical performances [13, 26] to the traditional Rosenberg's 1 or 2 femoral sockets ("bi-socket") procedure. This could have resulted in more

favorable clinical results [15] while the results remain controversial [19, 20].

According to the previous reports on the functional anatomy of the ACL, it could be divided into three bundles: the anteromedial (AM), the intermediate (IM), and the posterolateral (PL) [1, 17]. Additionally, it is well known that the natural ACL forms a crescent-shaped footprint on the femur and a triangular one on the tibia. Furthermore, in the double-bundle ACL reconstruction, the authors have found no graft implanted into the anterolateral portion of the tibial footprint (Fig. 1a). To closely mimic this normal structure and restore normal knee function, we have developed the triple-bundle ACL reconstruction [23]. As previously described, we have divided the "anteromedial graft" in the anatomical double-bundle ACL reconstruction into further two bundles (the AM and the IM grafts) to form a triangular shape in the tibial attachment (Fig. 1b) [23]. The aim of this study was to evaluate the morphology of the transplanted triple-bundle grafts by second-look arthroscopy.

Materials and methods

Between 2004 and 2006, the anatomical triple-bundle ACL reconstruction using semitendinosus tendon autograft was performed on 172 knees. Of those, second-look arthroscopy was performed on 42 knees in 42 patients who gave their informed consent. It has been our policy to recommend patients to undergo second-look arthroscopy as well as hardware removal. As the clinical record of one patient was incomplete, the other 41 patients were included in this study. Patients included 16 men and 25 women, with a mean age of 25.5 ± 8.5 years. The mean duration of follow-up was 11.4 ± 3.9 months. At the time of second-look arthroscopy, none of the patients complained of subjective instability. Lachman test was negative in 38 knees and mildly positive with a firm endpoint in 3 knees. Positive pivot shift test of +1 was found in one patient. The mean side-to-side difference with the KT-1000 arthrometer at maximum manual force was 0.7 ± 1.2 mm (Fig. 2).

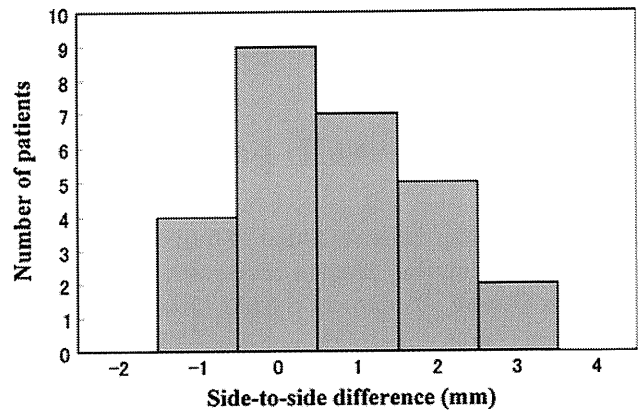

Fig. 2 The distribution of side-to-side differences in anterior laxity measured with the KT-1000 in 27 patients and the average value was 0.7 ± 1.2 mm

Surgical procedure

The procedure of triple-bundle ACL reconstruction was previously described in 2005 [23]. Briefly, two 2.4-mm guide pins were inserted to the points between the Resident's ridge and the posterior margin of the notch at 2, 3 o'clock for the left or at 9, 10 o'clock for the right knee using the anterolateral entry femoral aimer (Smith & Nephew Endoscopy, MA). For the tibia, three parallel guide pins were inserted using the offset parallel pin guide (Smith & Nephew Endoscopy, MA). Then, each wire was overdrilled with a drill bit of appropriate diameter (5–6 mm in diameter) (Fig. 3). After introducing the anteromedial and posterolateral grafts into each femoral tunnel, both the grafts were fixed with Endo-button CLs (Smith and Nephew Endoscopy, MA). For the tibial fixation, two double-spike plates (DSP; MEIRA Corp., Nagoya, JAPAN; US Patent No. 6117,139,21) and the tensioning boot were used as described [22, 23]. After the posterolateral graft and the two anterior graft sutures (the AM and IM) were tied to the DSPs, the tensioning sutures, which were applied to the bottom of the DSPs, were connected to the tensioners. The tensioners were mounted on the tensioning boot, which was affixed to the

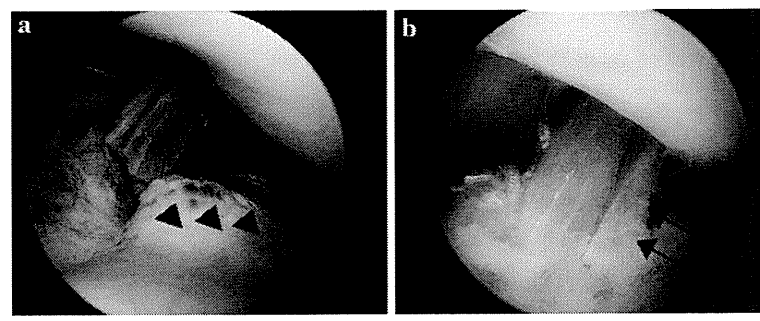

Fig. 1 Arthroscopic appearance of transplanted grafts in the left knee at the primary reconstruction. **a** Double-bundle reconstruction. Note the graft defect in the anterolateral portion of the tibial footprint (*arrowheads*). **b** Triple-bundle reconstruction. The intermediate graft occupies the anterolateral space (*arrows*)

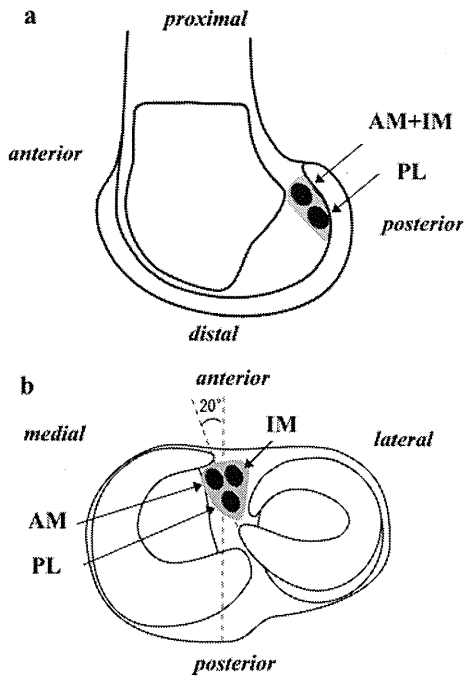

Fig. 3 Tunnel locations in the original ACL footprints (**a** femoral; **b** tibial): *AM* anteromedial, *IM* intermediate, *PL* posterolateral tunnel

tibia with a bandage. The 0.5 MPa of stress (approximately 10–15 N for each graft) was applied as the initial tension, and the knee was moved through a passive flexion and extension movement several times. After retighten tensioning suture by repetitive manual pulling to remove stress relaxation, each graft was fixed at 15–20° of knee flexion with DSPs and cancellous screws.

Postoperative rehabilitation

Postoperatively, the knee was immobilized with a brace for a week. Partial weight bearing was allowed at 3 weeks, followed by full weight bearing at 5 weeks. Jogging was allowed at 3 months and running was permitted at 4 months, followed by return to previous sports activity at 6–9 months.

Arthroscopic evaluation of the transplanted grafts

Arthroscopic evaluation of the grafts was performed by meticulous probing as described, focusing on tension and graft damage [10, 18, 25]. Tension of the graft was classified as taut or lax by probing at 20–90° of knee flexion. The grafts as tense as normal ACL throughout the range of motion were evaluated as taut, while those with grafts looser than the normal were evaluated as lax (Fig. 4). Graft damage was evaluated in each bundle and classified according to whether there was a substantial tear (Fig. 5). In addition, synovial coverage of the grafts was classified into the following 3 categories: "good," when the whole length of the graft was covered with the synovium; "fair," when more than 50% of the entire surface of the graft was

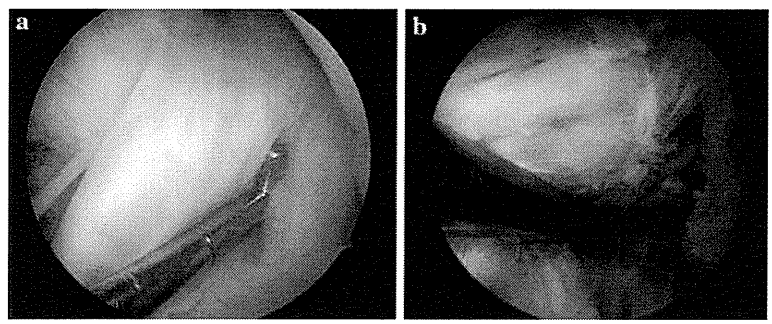

Fig. 4 Arthroscopic classification of transplanted grafts based on graft tension. **a** Taut AM, IM, and PL grafts. **b** Lax AM, IM, and PL grafts

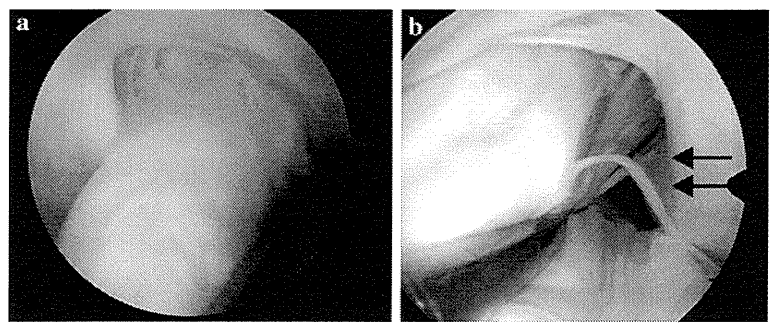

Fig. 5 Arthroscopic classification of transplanted grafts based on graft damage. **a** No rupture in all the grafts. **b** Complete rupture in the PL graft (*arrows*)

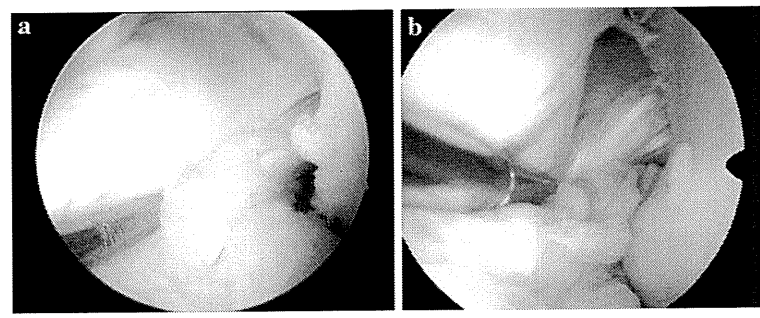

Fig. 6 Arthroscopic classification of transplanted grafts based on synovial coverage over the grafts. **a** "Good" synovial coverage in the AM and "Fair" in the IM. **b** "Poor" synovial coverage in the PL around the femoral tunnel aperture

covered with synovium; and "poor," when less than 50% of the graft showed synovial coverage (Fig. 6).

Correlation between morphological defects and clinical results

We examined whether these morphological defects in the PL grafts, including graft damage and incomplete synovial coverage, have an effect on clinical results at 2 years postoperatively.

Statistical analysis

The chi-square test and the Mann–Whitney U test were used for statistical analysis; a difference of $P < 0.05$ was considered significant.

Results

Graft morphology

All of the grafts showed more broad or "fan-out" shape approaching the tibial attachment (Fig. 7a). As to graft tension, 93% of the AM, 90% of the IM, and 88% of PL grafts were evaluated as taut, respectively. Significant differences in graft tension were not found among the three bundles (Table 1).

In terms of graft damage, there was no apparent rupture in the AM and IM grafts, while complete or substantial rupture was observed in 10% of the PL grafts around the femoral tunnel aperture (Fig. 5b). There was a significant difference in the incidence of graft damage among the three bundles ($P < 0.05$) (Table 1).

As to synovial coverage in the AM, thirty one grafts (76%) were evaluated as "Good," while five other grafts (12%) were evaluated as "Fair" and five (12%) as "Poor". In the IM grafts, 32 grafts (78%) were evaluated as "Good," five (12%) as "Fair," and four (10%) as "Poor". As to the PL, twenty-four grafts (59%) were evaluated as "Good," ten (24%) as "Fair," and seven (17%) as "Poor," respectively (Table 1). As a result, 41% of the PL grafts were not fully covered with synovium, while significant differences in the condition of synovial coverage were not found among the three bundles. In these cases, all of the synovial defects were observed around the femoral tunnel aperture, showing poor graft-tunnel integration (Fig. 6b).

Correlation between morphology of the PL graft and clinical results

After the arthroscopic evaluation, 22 of the patients could be followed up for 2 years after the reconstruction post-operatively and directly examined the correlation between

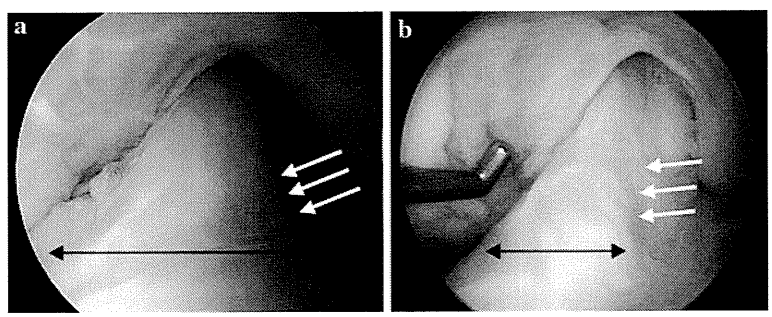

Fig. 7 Arthroscopic views of the multi-bundle ACL grafts. **a** A triple-bundle graft. Note the "fan-out" morphology approaching to the tibial attachment (*double-headed arrows*). **b** A double-bundle graft. Its anterior portion around the tibial attachment looks narrower (*double-headed arrows*). The *white arrows* show boundary between the anterior portion and the posterolateral of the graft

Table 1 Arthroscopic morphology of each graft

	Tension		Graft damage		Synovial coverage		
	Taut	Lax	−	+	Good	Fair	Poor
AM graft	38	3	41	0	31	5	5
	(93%)	(7%)	(100%)	(0%)	(76%)	(12%)	(12%)
IM graft	37	4	41	0	32	5	4
	(90%)	(10%)	(100%)	(0%)	(78%)	(12%)	(10%)
PL graft	36	5	37	4	24	10	7
	(88%)	(12%)	(90%)	(10%)	(59%)	(24%)	(17%)
P value	NS		0.016		NS		

morphology of the PL graft and clinical results among them.

According to IKDC subjective evaluation, 14 patients (64%) were graded as "normal" and the other eight patients (36%) as "nearly normal". There was no obvious deterioration throughout the follow-up period in the grade of Lachman test and pivot shift test in all of them. While three had showed apparent damage in the PL at the second-look arthroscopy, it did not make significant differences in the results of a subjective evaluation, Lachman test, pivot shift test, or KT measurement (Table 2). In terms of the synovial coverage of the PL, although those with incomplete synovial coverage at second-look arthroscopy revealed less favorable results in the subjective evaluation than those with complete coverage, no significant difference was found (Table 3). Similarly, the incomplete synovial coverage has not yet led to inferior results in Lachman and pivot shift tests at least 2 years postoperatively (Table 3).

Table 2 Correlation between graft damage of the PL graft and clinical results

	PL graft damage		*P* value
	− ($n = 19$)	+ ($n = 3$)	
IKDC subjective evaluation			NS
A (normal)	12	2	
B (nearly normal)	7	1	
C (abnormal)	0	0	
D (severely abnormal)	0	0	
Lachman test			NS
Normal	18	3	
1+	1	0	
2+	0	0	
Pivot shift test			NS
Negative	18	3	
Gliding	1	0	
Positive	0	0	
KT side-to-side difference (mm)	1.0 ± 1.3	0.0 ± 0.0	NS

Table 3 Correlation between synovial coverage of the PL graft and clinical results

	Synovial coverage		*P* value
	Good ($n = 13$)	Fair/poor ($n = 9$)	
IKDC subjective evaluation			NS
A (normal)	9	5	
B (nearly normal)	4	4	
C (abnormal)	0	0	
D (severely abnormal)	0	0	
Lachman test			NS
Normal	12	9	
1+	1	0	
2+	0	0	
Pivot shift test			NS
Negative	12	9	
Gliding	1	0	
Positive	0	0	
KT side-to-side difference (mm)	1.0 ± 1.5	0.7 ± 1.0	NS

Discussion

The most important finding of the present study was that the morphology of the triple-bundle grafts resembled that of the natural ACL. The natural ACL is composed of multiple fascicles, the basic unit of which is collagen. Each fascicle is composed of 3–20 subfasciculi that consist of groups of subfascicular unit [24]. It has been also described to be a complex anatomical structure where straight collagen bundles are formed by a complex network of interlacing fibrils [3]. To reproduce or mimic this multi-fascicular complex structure, current ACL reconstruction procedures are performed using multiple-bundle grafts.

Some authors have increasingly reported on an anatomical double-bundle ACL reconstruction, for it has several advantages to restore normal knee functions and to achieve successful results [13, 26]. Biomechanical study by Yagi et al. [26] revealed the importance of the anatomical reconstruction of both the anteromedial and the posterolateral bundle. Mae et al. [13] reported the study focusing on the laxity match pretension in which comparison was made in it between the anatomical double-bundle technique and the isometric bi-socket procedure and concluded that the former might restore the anterior stability more effectively than the latter.

In addition, it has been reported that the natural ACL consists of multiple bundles that share tensile force during knee motion [1, 2, 17]. Amis and Dawkins divided the ACL into three functional bundles (AM, IM, and PL bundles) and showed force distribution among these bundles [1]. The IM bundle shared approximately 30% of the